Numerical evaluation of various thermal management strategies for polymer electrolyte fuel cell stacks

Agus P. Sasmito [a,b,*], Erik Birgersson [a,b], Arun S. Mujumdar [a,c]

[a] Minerals Metals and Materials Technology Centre (M3TC), National University of Singapore, 9 Engineering Drive 1, Singapore 117576, Singapore
[b] Department of Chemical and Bio-Molecular Engineering, National University of Singapore, 5 Engineering Drive 2, Singapore 117576, Singapore
[c] Department of Mechanical Engineering, National University of Singapore, 9 Engineering Drive 1, Singapore 117576, Singapore

ARTICLE INFO

ABSTRACT

Thermal management is one of the key factors required to ensure good performance polymer electrolyte fuel cell (PEFC) stacks. The choice of the thermal management strategy depends on the specific application, size, weight, design, complexity, and cost. In this work, we investigate various alternative thermal management strategies for PEFC stacks, e.g., forced convection in specially design cooling plate/channel with either (i) liquid or (ii) air as the coolant; (iii) edge-air cooling with fins and; combine oxidant and coolant flow (open-cathode) with (iv) forced and (v) natural convection air cooling. A three-dimensional two-phase model, comprising of the equations of conservation of mass, momentum, species, energy and charge, is employed to quantify the performance of various cooling strategies. The results demonstrate that thermal management is essential to ensure good stack performance. Liquid cooling, as expected, performs the best compared to air cooling, whereas natural convection cooling is just marginally able to maintain a stack with large number of cells from steep drop in performance. Finally, results presented in this paper can provide useful design guidelines for selection of a suitable thermal management strategy for a PEFC stack and its near-to- or optimum cooling condition.

Copyright © 2011, Hydrogen Energy Publications, LLC. Published by Elsevier Ltd. All rights reserved.

1. Introduction

Thermal management is one of the important keys to efficient operation of polymer electrolyte membrane fuel cell (PEFC) stacks. In an ideal situation, each fuel cell in the stack would operate under identical operating condition; in reality, however, this is not feasible, as variations inevitably arise due to the design of stack manifold, position of the cell in the stack [1], and choice of thermal management strategy [2]. Efficient and cost-effective cooling of each cell in the stack is necessary to ensure high overall performance. If one removes too much heat, the reaction kinetics are adversely affected and, if water vapor partial pressure exceeds the saturation pressure, water vapor tends to condense which, in turn, lowers stack performance. Conversely, if cooling is not adequate, the stack temperature rises beyond its allowable operating temperature causing the membrane water content and its protonic conductivity to drop, which deteriorates stack performance. It

is therefore of interest to understand how various thermal management affect overall stack performance and which strategy to select for a given application.

Broadly speaking, depending on the type of the cathode manifold, the oxygen and/or air flow to the cathode can be supplied directly from ambient air (open-cathode) or through a gas manifold. For the former, ambient air is directly supplied to the cathode to provide both the oxidant as well as cooling air. The air flow can be provided by forced convection using a fan, or natural convection due to temperature gradient between the PEFC stack and the ambient. The former usually can be applied to stack with power rating up to sub kW, while the latter can only be used for small stacks of few cells (depends on the cell geometry) with power rating less than 100 W [3]. For a closed manifold stack, on the other hand, pure oxygen or air is usually supplied by forced convection through a stack manifold and is pre-conditioned, e.g., filtered, heated, and humidified. Therefore, an additional thermal management strategy is usually required. The most common cooling mechanism include forced convection in specially designed cooling plates/channels with either liquid or air as the coolant, edge-cooling with or without fins, and cooling coupled with phase-change materials used for thermal storage [4—7].

In practice, the choice of the thermal management strategy depends strongly on details of the specific application and its constraints; for example, in combined heat and fuel cell stationary power systems, liquid cooling (as illustrated in Fig. 1) is preferred since it has larger heat removal rate. Moreover, in this application there is no limitation on the size, weight and complexity of the system as it is used in stationary applications [2]. In small automotive and power generator applications where the weight, size and complexity of the system become the limiting factors, air cooling is preferred due to its simplicity as no coolant loop and heat exchanger are required by the system [8]. An open-cathode PEFC stack with natural convection cooling has been considered for portable

electronic power such as handphone power due to its simplicity [9].

Various cooling strategies for PEFC stacks have been studied experimentally; for example, stack with: liquid cooling [10—13], air cooling [14,15], edge-cooling [16], phase change cooling [17,18], combined oxidant and coolant flow [19—21], and natural convection cooling [22—24]. These experimental studies are useful in providing global understanding of the thermal management strategy with respect to stack performance. Reviews on the current status, challenges, opportunity, and research needed for thermal management in fuel cell stack can be found in [4—7]. In recent years, a number of mathematical models have been reported in the literature to model the transport phenomena occurring in a PEFC at the stack level [25—34]. Some studies focus only on fuel cell cooling without considering the electrochemistry aspects [35—38]. None of these studies, however, has considered a comprehensive comparative evaluation of the diverse thermal management strategies with respect to stack performance, parasitic load and complexity of design.

To extend the work on stack modeling and its thermal management strategy, the aim of the work presented here is threefold: first, to develop a comprehensive coupled three-dimensional mathematical model with several cooling strategies for a PEFC stack, coolant channel, ambient, fan and fins; second, to study the effect of cooling conditions, e.g., coolant flow rate, fan power rating, and buoyancy force (for natural convection cooling), with regard to the stack performance and thermal management; and third, to quantitatively compare five commonly used cooling strategies: closed manifold fuel cell stack with (i) liquid cooling, (ii) air cooling, and (iii) edge-cooling; and open-cathode fuel cell stack with (iv) forced and (v) natural convection for (a) single cell and (b) stack comprise of 12 cells, with respect to the stack performance, complexity of the design and parasitic load.

The layout of the paper is as follows. The comprehensive mechanistic mathematical model consist of fuel cell stack, coolant plates, ambient, fan and fins is introduced; it is comprised of two-phase conservation equations of mass, momentum, species, energy, charge, a phenomenological membrane model and agglomerate catalyst layer submodel. The model is then solved numerically using one-domain finite volume solver. Parameter studies for cooling conditions, e.g. coolant flow rate, fan power rating and buoyancy effect in the natural convection cooling at single cell and stack, are carried out to obtain near-to- or optimum operating condition The performance of five different cooling strategies are then compared with regard to the stack performance, complexity and parasitic load. Finally, conclusions are drawn and possible extension of the work for design optimization and selection are highlighted.

2.   Mathematical formulation

A one-domain two-phase flow model consisting of equations of conservation of mass, momentum, species, energy, and charge coupled with applicable electrochemistry and a phenomenological membrane model are solved for the fuel cell stack. Further extension of the stack model was carried out to account for the specific thermal management system,
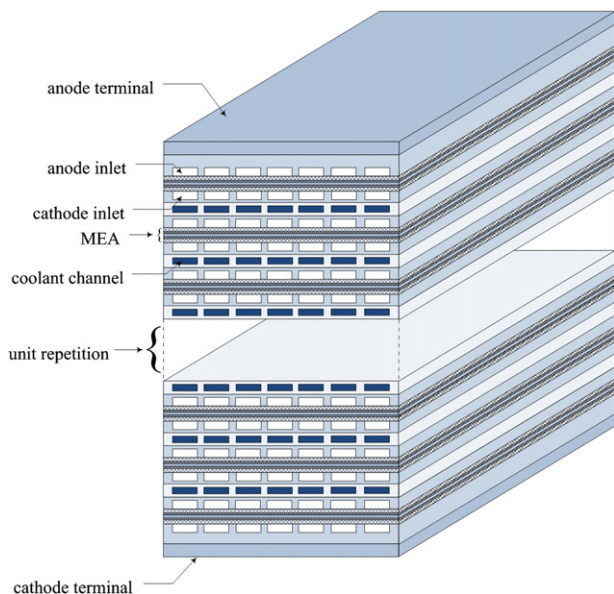

Fig. 1 — Schematic of PEFC stack.

e.g., coolant plates, fins, immediate ambient and fan. The model accounts for the following transport phenomena in each cell of the stack:

- *Mass, momentum and species transfer:* Conservation of two-phase mass, momentum and species is considered in the whole cell, with certain simplifications for the membrane. The gas phase consists of hydrogen, oxygen, water vapor and nitrogen, whereas the liquid phase is assumed to comprise only of liquid water due to the low solubility of the other gases.
- *Heat transfer:* The model considers convection, conduction, evaporation/condensation, ohmic heating, entropy generation and heat generation due to the activation overpotential.
- *Charge transfer:* Equations of conservation of charge and Ohm's law are solved.

The main model assumptions/approximations are:

- *Thermal equilibrium:* Local thermal equilibrium is assumed between all phases.
- *Membrane:* The membrane model takes into account the flux of water due to electroosmotic drag and diffusion. In this work, a GORE Primea 5510 membrane is employed for which we modify the standard phenomenological equations derived for a Nafion with a correction factor [31].
- *Two-phase flow:* It is assumed that the dominating driving force for liquid transport inside the gas diffusion layers and catalyst layers is capillarity. In the flow fields, we consider a mist flow approximation of the liquid flow, for which the liquid velocity is assumed to be the same as the gas velocity [31,32,39,40].
- *Catalyst layers:* An agglomerate model is implemented to account for mass transfer inside the cathode catalyst layer. Here, the agglomerate nucleus is assumed to be spherical in shape, which in turn is covered by a thin film of ionomer and water [31,32]. For the anode, a conventional expression based on the Butler−Volmer equation is employed as the overpotential is significantly lower than at the cathode.

2.1. Governing equations

The mathematical model consists of the conservation equations of momentum for steady laminar Newtonian fluid flow, together with conservation of energy, species, charge, and mass and a simplified two-phase flow model and phenomenological membrane model. Here, the superscripts (g), (l), (s), (m) and (cool) denote properties associated with the gas, liquid, solid, membrane and coolant, respectively, and (c) denotes any quantity associated with capillary pressure. For the sake of brevity; the constitutive relations and electrochemistry are summarized in Tables 1 and 2, respectively; while the boundary conditions are presented in Table 3.

2.1.1. Fuel cell stack
The conservation equations of mass, momentum, energy, species, charge, and two-phase flow are given by [31,32,39−41]:

$$\nabla \cdot \left(\rho^{(g)} \mathbf{u}^{(g)} \right) = S_{mass} - \dot{m}_{H_2O} \quad \text{(ff, gdl, cl)} \tag{1}$$

Table 1 − Constitutive relations.

$\rho^{(g)} = p^{(g)} M^{(g)} / RT$

$M^{(g)} = (\omega_{O_2}^{(g)}/M_{O_2} + \omega_{H_2}^{(g)}/M_{H_2} + \omega_{H_2O}^{(g)}/M_{H_2O} + \omega_{N_2}^{(g)}/M_{N_2})^{-1}$

$\omega_{N_2}^{(g)} = 1 - \omega_{H_2}^{(g)} - \omega_{O_2}^{(g)} - \omega_{H_2O}^{(g)}$

$x_i^{(g)} = \omega_i^{(g)} M^{(g)} / M_i$

$c_i^{(g)} = \omega_i^{(g)} \rho^{(g)} / M_i$

$\mathfrak{H} = p_{H_2O}^{(g)} / p_{H_2O}^{sat} \times 100$

$p_{H_2O}^{(g)} = x_{H_2O}^{(g)} p^{(g)}$

$p_{H_2O}^{sat} = p^{ref} \times 10^{c_1 + c_2(T - \mathfrak{T}_0) + c_3(T - \mathfrak{T}_0)^2 + c_4(T - \mathfrak{T}_0)^3}$

$\mu^{(g)} = \sum_\alpha x_\alpha^{(g)} \mu_\alpha^{(g)} / (\sum_\beta x_\beta^{(g)} \Phi_{\alpha\beta})$

$\Phi_{\alpha\beta} = 1/\sqrt{8}(1 + M_\alpha/M_\beta)^{-1/2} \left[1 + (\mu_\alpha/\mu_\beta)^{\frac{1}{2}} (M_\beta/M_\alpha)^{\frac{1}{4}} \right]^2$

$k^{(g)} = \sum_\alpha x_\alpha^{(g)} k_\alpha^{(g)} / (\sum_\beta x_\beta^{(g)} \Phi_{\alpha\beta})$

$k_{eff} = \varepsilon(1 - s)k^{(g)} + \varepsilon s k^{(l)} + (1 - \varepsilon)k^{(s)}$

$c_p^{(g)} = \sum_i \omega_i^{(g)} c_{p,i}^{(g)}$

$D_i^{(g)}(T, p^{(g)}) = (T/T_0)^{3/2}(p_0^{(g)}/p^{(g)})D_{i,0}^{(g)}(T_0, p_0^{(g)})$

$D_{i,eff}^{(g)} = (1 - s)\varepsilon^{3/2} D_i^{(g)}$

$\omega_{H_2O,a}^{in} = p_{H_2O}^{sat} M_{H_2O}(\mathfrak{H}_a^{in}/100)/(p^{(g)} M^{(g)})$

$\omega_{H_2O,c}^{in} = p_{H_2O}^{sat} M_{H_2O}(\mathfrak{H}_c^{in}/100)/(p^{(g)} M^{(g)})$

$\omega_{H_2,a}^{in} = 1 - \omega_{H_2O,a}^{in}$

$\omega_{O_2}^{in} = M_{O_2}/(1 + 79/21)[1/M^{(g)} - \omega_{H_2O}^{in}/M_{H_2O}]$

$i_{ave} = 1/A_{cl} \int \mathbf{i}^{(s)} dA_{cl}$

$\dot{m}_{H_2O} = c_r \max((1 - s)[p_{H_2O}^{(g)} - p_{H_2O}^{sat}]M_{H_2O}/(RT), /-s\rho^{(l)})$

$D^{(c)} = -\kappa s^3/\mu^{(l)} \dfrac{dp^{(c)}}{ds}$

$p^{(c)} = \tau \cos\theta \left(\dfrac{\varepsilon}{\kappa}\right)^{\frac{1}{2}} \mathcal{J}$

$\mathcal{J} = 1.417(1 - s) - 2.12(1 - s)^2 + 1.263(1 - s)^3$

$\lambda = \begin{cases} 0.043 + 17.81a^2 + 36.0a^3 & a \leq 1 \\ 14 + 1.4(a - 1) & 1 \leq a \leq 3 \end{cases}$

$a = p_{H_2O}^{(g)}/p_{H_2O}^{sat} + 2s$

$\sigma_{eff}^{(m)} = \beta^{(m)}(0.5193\lambda - 0.326)\exp[1268(1/303.15 - 1/T)]$

$D_{H_2O,eff}^{(m)} = \beta^{(m)} \begin{cases} 3.1 \times 10^{-7} \times \lambda[\exp(0.28\lambda) - 1]\exp(-2436/T) & \text{for } \lambda > 3 \\ 4.17 \times 10^{-8} \times \lambda[1 + 161\exp(-\lambda)]\exp(-2436/T) & \text{for } \lambda > 3 \end{cases}$

$n_d = 2.5\lambda/22$

$$\nabla \cdot \left(\rho^{(l)} \mathbf{u}^{(l)} \right) = \dot{m}_{H_2O} \quad \text{(ff, gdl, cl)} \tag{2}$$

$$\nabla \cdot \left(\rho^{(g)} \mathbf{u}^{(g)} \mathbf{u}^{(g)} \right) = \nabla \cdot \sigma + S_{mom} \quad \text{(ff, gdl, cl)} \tag{3}$$

$$\nabla \cdot \left(\rho^{(g)} C_p^{(g)} \mathbf{u}^{(g)} T \right) = \nabla \cdot \left(k_{eff} \nabla T \right) + S_{temp} \quad \text{(sp, ff, gdl, cl, m)} \tag{4}$$

$$\nabla \cdot \mathbf{n}_i^{(g)} = S_i \quad \text{(ff, gdl, cl)} \tag{5}$$

$$\nabla \cdot \mathbf{n}_{H_2O}^{(m)} = 0 \quad \text{(m)} \tag{6}$$

$$\nabla \cdot \mathbf{i}^{(m)} = S_{pot} \quad \text{(cl, m)} \tag{7}$$

$$\nabla \cdot \mathbf{i}^{(s)} = -S_{pot} \quad \text{(sp, ff, gdl, cl)} \tag{8}$$

In the above set of equations, $\rho^{(g, l)}$ represents phase densities, $\mathbf{u}^{(g, l)} = (u^{(g, l)}, v^{(g, l)}, w^{(g, l)})$ are the phase velocities (in the x, y and z directions), $\dot{m}_{H_2O}$ is the interphase mass transfer of

Table 2 – Electrochemistry & agglomerate model.

$$J_a = j_a^{ref}(c_{H_2}^{(g)}/c_{H_2,ref}^{(g)})^{1/2}[\exp(\alpha_a^{ox}F\eta_a/(RT)) - \exp(-\alpha_c^{ox}F\eta_a/(RT))]$$

$$J_c = j_c^{ref}(c_{O_2}^{(g)}/c_{O_2,ref}^{(g)})[-\exp(\alpha_a^{rd}F\eta_c/(RT)) + \exp(-\alpha_c^{rd}F\eta_c/(RT))]$$
$$\times (1 - \gamma_{cl})(1 - \gamma^{(p)}/\gamma^{(agg)})RT/H_{O_2}^{(p)}\xi_1/(1 + \xi_2 + \xi_3)$$

$$j_c^{ref} = j_{c,0}^{ref}\exp[-E_a/R(1/T - 1/\mathfrak{T}_1)]$$

$$c_{i,ref}^{(g)} = p^{ref}/H_i^{(p)}$$

$$\eta_a = \phi^{(s)} - \phi^{(m)}$$

$$\eta_c = \phi^{(s)} - \phi^{(m)} - E_{rev}$$

$$E_{rev} = E_{rev,0} + \mathfrak{t}_1(T - \mathfrak{T}_2) + RT/(4F)\ln x_{O_2}^{(g)}$$

$$\xi_1 = 1/\Phi[1/(\tanh(3\Phi)) - 1/(3\Phi)]$$

$$\xi_2 = \delta^{(p)}\xi_1 k_c/(D_{O_2}^{(p)}a^{(p)})$$

$$\xi_3 = \delta^{(l)}\xi_1 k_c/(D_{O_2}^{(l)}a^{(l)}) \times H_{O_2}^{(l)}/H_{O_2}^{(p)}$$

$$\Phi = r^{(agg)}\Big/3\sqrt{k_c/D_{O_2,eff}^{(agg)}}$$

$$k_c = j_c^{ref}(1 - \gamma^{(p)}/\gamma^{(agg)})(-\exp(\alpha_a^{rd}F\eta_c/(RT))$$
$$+ \exp(-\alpha_c^{rd}F\eta_c/(RT)))/(4Fc_{O_2,ref}^{(g)})$$

$$D_{O_2,eff}^{(agg)} = DO_2^{(p)}(\gamma^{(p)}/\gamma^{(agg)})^{1.5}$$

$$\delta^{(p)} = \sqrt[3]{(r^{(agg)})^3(1 + \gamma^{(p)}/\gamma^{(PtC)})} - r^{(agg)}$$

$$\delta^{(l)} = \sqrt[3]{(r^{(agg)} + \delta^{(p)})^3(1 + \gamma^{(l)}/\gamma^{(agg)})} - (r^{(agg)} + \delta^{(p)})$$

$$a^{(p)} = 4\pi n^{(agg)}(r^{(agg)} + \delta^{(p)})^2$$

$$a^{(l)} = 4\pi n^{(agg)}(r^{(agg)} + \delta^{(p)} + \delta^{(l)})^2$$

$$n^{(agg)} = 3/(4\pi) \times \gamma^{(agg)}/((r^{(agg)} + \delta^{(p)})^3)$$

$$\gamma^{(agg)} = V^{(agg)}/V_{tot} = \gamma^{(p)} + \gamma^{(PtC)}$$

$$\gamma_{cl} = V_{void}/V_{tot} = 1 - \gamma^{(agg)}$$

$$\gamma^{(p)} = V^{(p)}/V_{tot} = \omega^{(p)}/(1 - \omega^{(p)}) \times \mathfrak{L}^{(Pt)}/(\rho^{(m)}h_{cl}\omega^{(Pt)})$$

$$\gamma^{(PtC)} = V^{(PtC)}/V_{tot} = [1/\rho^{(Pt)} + (1 - \omega^{(Pt)})/(\rho^{(C)}\omega^{(Pt)})]\mathfrak{L}^{(Pt)}/h_{cl}$$

$$\gamma^{(l)} = V^{(l)}/V_{tot} = s\gamma_{cl}$$

$$\omega^{(p)} = \mathfrak{L}^{(p)}/(\mathfrak{L}^{(Pt)} + \mathfrak{L}^{(C)} + \mathfrak{L}^{(p)})$$

$$\omega^{(Pt)} = \mathfrak{L}^{(Pt)}/(\mathfrak{L}^{(C)} + \mathfrak{L}^{(Pt)})$$

$$V^{(agg)} = V^{(PtC)} + V^{(p)}$$

$$V_{tot} = V^{(agg)} + V_{void} = V^{(PtC)} + V^{(p)} + V^{(g)} + V^{(l)}$$

$$V_{void} = V^{(g)} + V^{(l)}$$

water between the gas and the liquid phase, $\boldsymbol{\sigma}$ is the total stress tensor [42], $\mu^{(g,l)}$ are the phase dynamic viscosities, $C_p^{(g)}$ is the specific heat capacity, T is the temperature, and k_{eff} is the effective thermal conductivity, and $\mathbf{n}_i^{(g)}$ is the mass

flux of species i, while $\mathbf{n}_{H_2O}^{(m)}$ is the water flux in the membrane. Furthermore, $\mathbf{i}^{(m)}$ and $\mathbf{i}^{(s)}$ represent the current densities carried by protons and electrons respectively. The mass fluxes of species, current densities, liquid water velocity and total stress tensor are defined as follows [31,32,39,40]:

$$\mathbf{n}_i^{(g)} = \rho^{(g)}\mathbf{u}^{(g)}\omega_i^{(g)} - \rho^{(g)}D_{i,eff}^{(g)}\nabla\omega_i^{(g)} \quad (i = H_2, O_2, H_2O, N_2) \tag{9}$$

$$\mathbf{n}_{H_2O}^{(m)} = \frac{n_d M_{H_2O}}{F}\mathbf{i}^{(m)} - \frac{\rho^{(m)}}{M^{(m)}}M_{H_2O}D_{H_2O,eff}^{(m)}\nabla\lambda \tag{10}$$

$$\mathbf{i}^{(m)} = -\sigma_{eff}^{(m)}\nabla\phi^{(m)} \tag{11}$$

$$\mathbf{i}^{(s)} = -\sigma_{eff}^{(s)}\nabla\phi^{(s)} \tag{12}$$

$$\mathbf{u}^{(l)} = \begin{cases} \mathbf{u}^{(g)}s - D^{(c)}\nabla s & \text{(ff)} \\ -D^{(c)}\nabla s & \text{(gdl, cl)} \end{cases} \tag{13}$$

$$\boldsymbol{\sigma} = -p^{(g)}I + \mu^{(g)}\Big[\nabla\mathbf{u}^{(g)} + (\nabla\mathbf{u}^{(g)})^T\Big] - \frac{2}{3}\mu^{(g)}(\nabla\cdot\mathbf{u}^{(g)})I \tag{14}$$

The numerical model solves for a species mixture consisting of hydrogen (H_2), water (H_2O), oxygen (O_2) and nitrogen (N_2) in the whole domain (note that the hydrogen and oxygen concentrations in the cathode and anode are set to near-zero numerically); $\omega_i^{(g)}$ denotes the mass fraction of species i in the gas phase, and $D_{i,eff}^{(g)}$ represents the effective diffusivity in the gas phase. The flux of water in the membrane, Eq. (10), is expressed by a phenomenological model (43) in terms of the membrane water content, λ, which accounts for the electro-osmotic drag (first term on the right hand side [RHS]) and diffusion (second term on the RHS). Here, $D_{H_2O,eff}^{(m)}$ is the effective diffusivity of water in the membrane, F is Faraday's constant, M_{H_2O} denotes the molecular mass of water, n_d is the electroosmotic drag coefficient, $\rho^{(m)}$ and $M^{(m)}$ are the density and equivalent weight of the dry membrane respectively. In Eqs. 11 and 12, $\varphi^{(m)}$ and $\varphi^{(s)}$ represent the potentials of the ionic phase and the solid phase respectively, while $\sigma_{eff}^{(m)}$ and $\sigma_{eff}^{(s)}$ are the effective electrical conductivities of proton and electron transport respectively. In Eq. (13), s is the liquid saturation and

Table 3 – Boundary conditions.

At the ambient front (case iii, iv, v)	$p^{(g)} = p^{amb}, \omega_{O_2}^{(g)} = \omega_{O_2}^{amb}, \omega_{H_2O}^{(g)} = \omega_{H_2O}^{amb}, T = T^{amb}, s = 0$
At the ambient rear (case iii, iv, v)	$p^{(g)} = p^{ref}, (e_z\cdot\nabla)(u^{(g)}\cdot e_x) = 0, (e_z\cdot\nabla)(u^{(g)}\cdot e_y) = 0, e_z\cdot\nabla\omega_i^{(g)} = 0, e_z\cdot\nabla T = 0, e_z\cdot\nabla s = 0$
At the anode inlet (all cases)	$u^{(g)}\cdot e_z = u_a^{in}, \omega_{H_2}^{(g)} = \omega_{H_2,a}^{in}, \omega_{H_2O}^{(g)} = \omega_{H_2O,a}^{in}, T = T_a^{in}, s = 0$
At the anode outlet (all cases)	$p^{(g)} = p^{ref}, (e_z\cdot\nabla)(u^{(g)}\cdot e_x) = 0, (e_z\cdot\nabla)(u^{(g)}\cdot e_y) = 0, e_z\cdot\nabla\omega_i^{(g)} = 0, e_z\cdot\nabla T = 0, e_z\cdot\nabla s = 0$
At the cathode inlet (case i, ii, iii)	$u^{(g)}\cdot e_z = u_c^{in}, \omega_{O_2}^{(g)} = \omega_{O_2,c}^{in}, \omega_{H_2O}^{(g)} = \omega_{H_2O,c}^{in}, T = T_c^{in}, s = 0$
At the cathode outlet (case i, ii, iii)	$p^{(g)} = p^{ref}, (e_z\cdot\nabla)(u^{(g)}\cdot e_x) = 0, (e_z\cdot\nabla)(u^{(g)}\cdot e_y) = 0, e_z\cdot\nabla\omega_i^{(g)} = 0, e_z\cdot\nabla T = 0, e_z\cdot\nabla s = 0$
At the coolant inlet (case i, ii)	$u^{(cool)}\cdot e_z = u_{cool}^{in}, T = T_{cool}^{in}$
At the coolant outlet (case i, ii)	$p^{(cool)} = p^{ref}, (e_z\cdot\nabla)(u^{(cool)}\cdot e_x) = (e_z\cdot\nabla)(u^{(cool)}\cdot e_y) = e_z\cdot\nabla T = 0$
At the lower boundary (case i, ii, iii)	$\phi^{(s)} = E_{cell}, p_{-y}^{(g)} = p_{+y}^{(g)}, u_{-y}^{(g)} = u_{+y}^{(g)}, \omega_{i,-y}^{(g)} = \omega_{i,+y}^{(g)}, T_{-y} = T_{+y}, s_{-y} = s_{+y}$
At the upper boundary (case i, ii, iii)	$\phi^{(s)} = 0, p_{+y}^{(g)} = p_{-y}^{(g)}, u_{+y}^{(g)} = u_{-y}^{(g)}, \omega_{i,+y}^{(g)} = \omega_{i,-y}^{(g)}, T_{+y} = T_{-y}, s_{+y} = s_{-y}$
At the symmetry (all cases)	$(n\cdot\nabla)(u^{(g)}\cdot t) = 0, n\cdot u^{(g)} = 0, n\cdot\nabla\omega_i^{(g)} = 0, n\cdot\nabla T = 0, n\cdot\nabla s = 0, n\cdot\nabla\phi^{(s)} = 0, n\cdot\nabla\phi^{(m)} = 0$
At the walls (all cases)	$u^{(g)} = 0, n\cdot\nabla\omega_i^{(g)} = 0, n\cdot\nabla T = 0, n\nabla s = 0, n\cdot\nabla\phi^{(s)} = 0, n\cdot\nabla\phi^{(m)} = 0$

$D^{(c)}$ is the capillary diffusion. For the total stress tensor, Eq. (14), $p^{(g)}$ is the gas pressure and $\mathbf{I}$ is the identity matrix. The source terms in Eqs. (1)–(8) are given by [31,32,39,40]

$$S_{\text{mass}} = \begin{cases} -\dfrac{M_{O_2}J_c}{4F} + \dfrac{M_{H_2O}J_c}{2F} - \nabla \cdot \mathbf{n}_{H_2O}^{(m)} & \text{(cathode cl)} \\[2mm] -\dfrac{M_{H_2}J_a}{2F} - \nabla \cdot \mathbf{n}_{H_2O}^{(m)} & \text{(anode cl)} \\[2mm] 0 & \text{(elsewhere)} \end{cases} \tag{15}$$

$$\mathbf{S}_{\text{mom}} = \begin{cases} -\dfrac{\mu^{(g)}}{\kappa}\mathbf{u}^{(g)} & \text{(gdl, cl)} \\[2mm] 0 & \text{(elsewhere)} \\[2mm] \rho^{(g)}\mathbf{g} & \text{(case }(v)\text{)} \end{cases} \tag{16}$$

$$S_i = \begin{cases} -\dfrac{M_{O_2}J_c}{4F} & (O_2, \text{ cathode cl}) \\[2mm] +\dfrac{M_{H_2O}J_c}{2F} - \nabla \cdot \mathbf{n}_{H_2O}^{(m)} - \dot{m}_{H_2O} & (H_2O, \text{ cathode cl}) \\[2mm] -\nabla \cdot \mathbf{n}_{H_2O}^{(m)} - \dot{m}_{H_2O} & (H_2O, \text{ anode cl}) \\[2mm] -\dfrac{M_{H_2}J_a}{2F} & (H_2, \text{ anode cl}) \\[2mm] 0 & \text{(elsewhere)} \end{cases} \tag{17}$$

$$S_{\text{pot}} = \begin{cases} -j_c & \text{(cathode cl)} \\[1mm] j_a & \text{(anode cl)} \\[1mm] 0 & \text{(elsewhere)} \end{cases} \tag{18}$$

$$S_{\text{temp}} = \begin{cases} J_c\left(-T\dfrac{\partial E_{\text{rev}}}{\partial T} + |\eta_c|\right) + \sigma_{\text{eff}}^{(m)}\left(\nabla\phi^{(m)}\right)^2 \\[1mm] \qquad + \sigma_{\text{eff}}^{(s)}\left(\nabla\phi^{(s)}\right)^2 + \dot{m}_{H_2O}H_{\text{vap}} & \text{(cathode cl)} \\[2mm] J_a\eta_a + \sigma_{\text{eff}}^{(m)}\left(\nabla\phi^{(m)}\right)^2 + + \sigma_{\text{eff}}^{(s)}\left(\nabla\phi^{(s)}\right)^2 + \dot{m}_{H_2O}H_{\text{vap}} & \text{(anode cl)} \\[2mm] \sigma_{\text{eff}}^{(m)}\left(\nabla\phi^{(m)}\right)^2 & \text{(m)} \\[2mm] \sigma_{\text{eff}}^{(s)}\left(\nabla\phi^{(s)}\right)^2 + \dot{m}_{H_2O}H_{\text{vap}} & \text{(gdl)} \\[2mm] \sigma_{\text{eff}}^{(s)}\left(\nabla\phi^{(s)}\right)^2 & \text{(ff, sp)} \end{cases} \tag{19}$$

The source term for mass conservation, S_{mass}, comprises of mass consumption and production due to electrochemical reactions and transport of water through the membrane, whilst the source terms for species conservation, S_i, consider species consumption and production due to electrochemical reactions as well as interphase mass transfer for water and the transport of water through the membrane [40]. In the first entry of Eq. (4), the first two terms are the reversible and irreversible entropic heat generated by the electrochemical reaction [44], the third and fourth terms describe ohmic heating, whereas the energy transfer due to interphase mass transfer is described in the last term, where H_{vap} is the heat of vaporization of water. In Eq. (3), $J_{a, c}$ ($J_{a, c} > 0$) denote the volumetric current densities, E_{rev} is the reversible potential, η_a ($\eta_a > 0$) and η_c ($\eta_c < 0$) are the overpotentials at the anode and cathode.

2.1.2. Ambient

The model solves the differential equations of conservation of mass (gas and liquid), momentum, species and energy

$$\nabla \cdot \left(\rho^{(g)}\mathbf{u}^{(g)}\right) = 0 \tag{20}$$

$$\nabla \cdot \left(\rho^{(1)}\mathbf{u}^{(1)}\right) = 0 \tag{21}$$

$$\nabla \cdot \left(\rho^{(g)}\mathbf{u}^{(g)}\mathbf{u}^{(g)}\right) = \nabla \cdot \boldsymbol{\sigma} + \mathbf{S}_{\text{mom}} \tag{22}$$

$$\nabla \cdot \mathbf{n}_i^{(g)} = 0 \tag{23}$$

$$\nabla \cdot \left(\rho^{(g)}c_p^{(g)}\mathbf{u}^{(g)}T\right) = \nabla \cdot \left(k_{\text{eff}}\nabla T\right) \tag{24}$$

where the mass flux for species, liquid water velocities and total stress tensor are defined as

$$\mathbf{n}_i^{(g)} = \rho^{(g)}\mathbf{u}^{(g)}\omega_i^{(g)} - \rho^{(g)}D_{i,\text{eff}}^{(g)}\nabla\omega_i^{(g)}, (i = H_2O, O_2, N_2) \tag{25}$$

$$\mathbf{u}^{(1)} = \mathbf{u}^{(g)}s \tag{26}$$

$$\boldsymbol{\sigma} = -p^{(g)}\mathbf{I} + \mu^{(g)}\left[\nabla\mathbf{u}^{(g)} + \left(\nabla\mathbf{u}^{(g)}\right)^{\text{T}}\right] - \frac{2}{3}\mu^{(g)}\left(\nabla\cdot\mathbf{u}^{(g)}\right)\mathbf{I} \tag{27}$$

$$\mathbf{S}_{\text{mom}} = \rho^{(g)}\mathbf{g}, \text{ (for case}(v)) \tag{28}$$

2.1.3. Fan

The fan model is based on the fan characteristic curve which is used as an interfacial condition; the model is represented by a polynomial function that is fitted to data from the manufacturer for the static pressure increase over the fan vis-a-vis the flow velocities based on the average conditions at the fan. The overall velocity that is achieved by the fan is thus not known a priori but needs to be iterated for. The polynomial function is defined by [32]

$$\Delta p_{\text{fan}} = \mathfrak{C}_1\left(u_{\text{fan}}\right)^7 + \mathfrak{C}_2\left(u_{\text{fan}}\right)^6 + \mathfrak{C}_3\left(u_{\text{fan}}\right)^5 + \mathfrak{C}_4\left(u_{\text{fan}}\right)^4 \\ + \mathfrak{C}_5\left(u_{\text{fan}}\right)^3 + \mathfrak{C}_6\left(u_{\text{fan}}\right)^2 + \mathfrak{C}_7 u_{\text{fan}} + \mathfrak{C}_8 \tag{29}$$

where $\mathfrak{C}_i$ are parameter-adapted constants, Δp_{fan} is the static pressure increase over the fan, and u_{fan} is the velocity through the fan. Note that arbitrary fan(s) can be implemented in the simulation once the fan characteristic curve is known.

2.1.4. Coolant plates

The model solves for the conservation of mass, momentum, and energy in the coolant plates (31)

$$\nabla \cdot \left(\rho^{(\text{cool})}\mathbf{u}^{(\text{cool})}\right) = 0 \tag{30}$$

$$\nabla \cdot \left(\rho^{(\text{cool})}\mathbf{u}^{(\text{cool})}\mathbf{u}^{(\text{cool})}\right) = \nabla \cdot \boldsymbol{\sigma} \tag{31}$$

$$\nabla \cdot \left(\rho^{(\text{cool})}c_p^{(\text{cool})}\mathbf{u}^{(\text{cool})}T\right) = \nabla \cdot \left(k_{\text{eff}}\nabla T\right) \tag{32}$$

where the total stress tensor are defined as

$$\boldsymbol{\sigma} = -p^{(\text{cool})}\mathbf{I} + \mu^{(\text{cool})}\left[\nabla\mathbf{u}^{(\text{cool})} + \left(\nabla\mathbf{u}^{(\text{cool})}\right)^{\text{T}}\right] \tag{33}$$

2.1.5. Fins

The model solves for anisotropic heat conduction in the fins similar to [16]

$$\nabla \cdot \left(k_{\text{fin}} \nabla T \right) = 0 \tag{34}$$

2.2. Thermal management strategies

For detailed implementation of various thermal management strategies, the following procedure were employed to ensure consistency between physical model and its mathematical counterpart:

- Case (i): closed manifold PEFC stack with liquid cooling applied at the top and bottom of every cell in the stack. The coolant and gas channels are assumed to be parallel channel running in co-flow mode. The computational cost is kept to a minimum by introducing a representative computational domain with symmetry boundary conditions to the left and right and periodic boundary conditions at the upper and lower parts; the latter represent a unit repetition of stack, as illustrated in Fig. 2a.
- Case (ii): closed manifold PEFC stack with air cooling at the top and bottom of every cell in the stack. The model is similar to case (i) except that the coolant fluid is air (see Fig. 2a). A more details discussion on the mathematical model and its assumption for case (i) and (ii) can be found in our previous work [31], for which it is now extended to account for three-dimensional effect of parallel flow channel.
- Case (iii): closed manifold PEFC stack with edge-air cooling. The computational domain is illustrated in Fig. 2b, where a unit repetition with periodic boundary condition is applied at the top and bottom of the cell; and symmetry boundary condition to the middle of the stack is considered to reduce the computational cost. Moreover, the model is also solved for fan, fins, and its immediate ambient at the front, rear and in between fins area. Note that this is the first comprehensive mechanistic model available in literature which completely account for the fuel cell stack, ambient, fan and anisotropic conductive heat transfer in fins.
- Case (iv): open-cathode PEFC stack with forced air-convection powered by fan. The model considers the whole stack with 12 cells, fan and its immediate ambient, as shown in Fig. 2c. The flow channels are assumed to be parallel running in co-flow mode which can be approximated by symmetric boundary at mid-plane of the channel, similar to previous work [45]. A detailed discussion of the mathematical model can be found in [32] which is now extended for the first time to account for whole stack without unit repetition, ambient and fan as well as taken into account for the three-dimensional effect of parallel flow channel.
- Case (v): open-cathode PEFC: a) single cell and b) stack comprising 12 cells with natural convection air cooling. The computational domain is similar to case (iv) except that there is no fan included in the model. The dominant flow mechanism is therefore the buoyancy force due to gravity and temperature gradient between fuel cell and ambient.

The models consisting of the governing conservation equations, constitutive relations, and boundary conditions are then solved numerically.

3. Numerics

The computational domains (see Fig. 2) were created and meshed using the pre-processor software Gambit 2.3.16 [46]. After mesh independence study, the computational domains were resolved with $\sim 8 \times 10^4$ elements for case (i) and (ii), $\sim 4 \times 10^5$ elements for case (iii), $\sim 4.5 \times 10^5$ elements for case (iv) and (v). To further reduce the computational cost, a fine *structured* mesh inside the PEFC stack and increasingly coarser *unstructured* mesh in the ambient air are considered for case (iii)–(v). The mathematical models for stack, coolant plates, ambient and fan comprising of 12 dependent variables—$p^{(g)}$, $u^{(g)}$, $v^{(g)}$, $w^{(g)}$, $\omega_{H_2}^{(g)}$, $\omega_{O_2}^{(g)}$, $\omega_{H_2O}^{(g)}$, T, $\varphi^{(s)}$, $\varphi^{(m)}$, s, and λ—were then implemented in the commercial computational fluid dynamics software Fluent 6.3 [46] and its fuel cell module. It is further customized with User Defined Functions (UDF) written in C language to account for agglomerate catalyst layer model, membrane model setting, heat generation in the catalyst layer and boundary conditions. The set of partial differential equations were solved using the SIMPLE algorithm; second-order upwind discretization for the conservation of momentum, species, and energy; and first-order upwind discretization for the conservation of charge, liquid water and membrane water content. In addition, body force weighted discretization is applied for momentum conservation for case (v). As indication of computational cost, it is noted that on average, around 200 to 1000 iterations are needed for a convergence criteria for all the relative residual of 10^{-6}; these take about 10–20 min for case (i) and (ii), 1–2 h for case (iii), and 2–3 h for case (iv) and (v) on a workstation with a quad-core processor (2.6 GHz) without parallelization. Note that within these computational time-frame, and further improved with parallelization scheme, the model presented herein can be easily employed for designs and optimization purposes.

4. Results and discussion

For each thermal management strategy, simulations were carried out for typical conditions found in a PEFC stack: a fully humidified fuel and oxidant are supplied to both anode and cathode with constant inlet velocity for closed manifold stacks; whereas, for open-cathode, the fuel (hydrogen) is assumed to be fully humidified, while the oxidant is directly supplied from air at typical ambient conditions. Furthermore, the coolant conditions are also assumed to be those found in typical conditions; that is the inlet coolant temperature for case (i) is assumed to be the same as the operating temperature, and for air-based cooling (case (ii)–(v)), typical ambient air is used to cool down the stack. The electrochemical parameters were calibrated and validated against experimental polarization curves and local current density distributions in our previous work [31] obtained from a segmented PEFC with liquid cooling at the top and bottom of the cell. The representative computational unit cell for stack is identical to the validation case, except that the flow channel is of parallel channel and the thermal management strategy is modified for
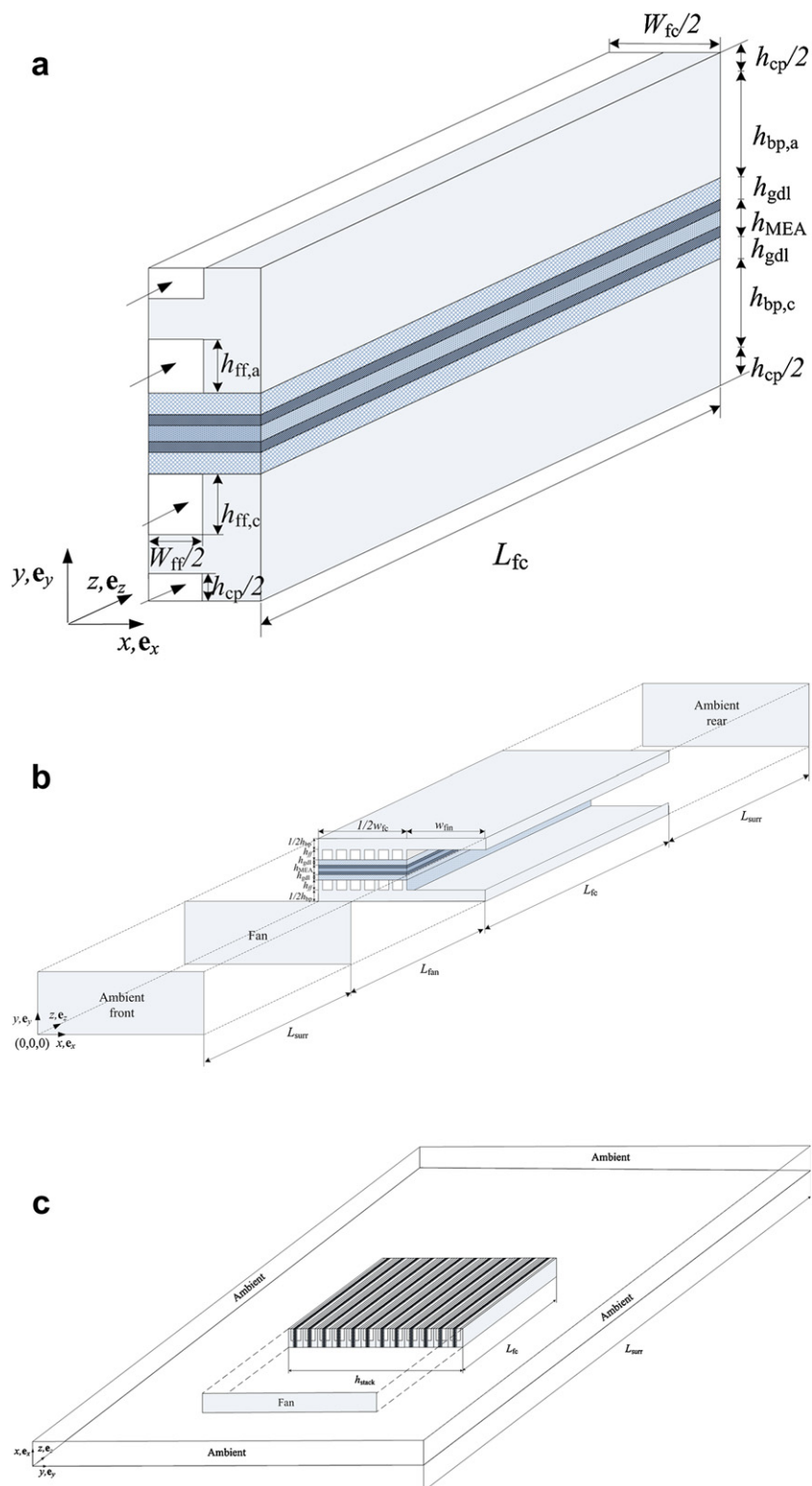
Fig. 2 — Computational domain for a) case i and ii; b) case iii; and c) case iv and v.

Table 4 – Base-case parameters.

Parameter	Value	Units	Reference
$c_{p,H_2}^{(g)}, c_{p,H_2O}^{(g)}, c_{p,O_2}^{(g)}, c_{p,N_2}^{(g)}$	$(14.283, 2.014, 0.919, 1.041) \times 10^3$	J kg^{-1} K^{-1}	–
c_r	100	s^{-1}	[55]
$D_{H_2,0}^{(g)}, D_{H_2O,0}^{(g)}, D_{O_2,0}^{(g)}$	$(11.03, 7.35, 3.23) \times 10^{-5}$	m^2 s^{-1}	[56]
$D_{O_2}^{(1)}$	3.032×10^{-9}	m^2 s^{-1}	[57, 58]
$D_{O_2}^{(p)}$	$4{:}38 \times 10^{-6} \exp(-23848/RT)$	m^2 s^{-1}	[59, 60]
E_a	73269	J mol^{-1}	[59]
$E_{cell}, E_{rev},0$	0.9–0.3, 1.23	V	–, [56]
F	96487	C mol^{-1}	–
$H_{H_2}^{(p)}$	$2.58 \times 10^3 \exp(170/T)$	Pa m^3 mol^{-1}	[61]
$H_{O_2}^{(p)}$	$1.34 \times 10^5 \exp(-666/T)$	Pa m^3 mol^{-1}	[62]
$H_{O_2}^{(l)}$	$5.14 \times 10^5 \exp(-498/T)$	Pa m^3 mol^{-1}	[62]
H_{vap}	2.26×10^6	J kg^{-1}	[63]
$h_{cl}, h_{ff}, h_{gdl}, h_m, h_{bp}$	$(0.01, 0.5; 0.3, 0.05, 1) \times 10^{-3}$	m	[54]
j_a^{ref}, j_c^{ref}	$10^9, 275$	A m^{-3}	[31,56]
$k_{cl}^{(s)}, k_{ff}^{(s)}, k_{gdl}^{(s)}, k_m^{(s)}, k_{bp}^{(s)}$	1.5, 13.3, 1.5, 0.2, 16.3	W m^{-1} K^{-1}	[54,64–66]
$k_{fin.x}, k_{fin.y}, k_{fin.z}$	290, 290, 3.5	W m^{-1} K^{-1}	[16]
$k_{H_2}^{(g)}, k_{H_2O}^{(g)}, k_{N_2}^{(g)}, k_{O_2}^{(g)}, k^{(1)}$	$(20.28, 2.16, 2{:}82, 2.89, 67) \times 10^{-2}$	W m^{-1} K^{-1}	[67]
L, L_{fan}, L_{surr}	$(9, 1,18) \times 10^{-2}$	m	[54], –, –
$M_{H_2}, M_{H_2O}, M_{O_2}, M_{N_2}$	$(2, 18, 32, 28) \times 10^{-3}$	kg mol^{-1}	–
$M^{(m)}$	1.1	kg mol^{-1}	[56]
$p^{amb}, p^{ref}, p_0^{(g)}$	101325, 101325, 101325	Pa	[54,68]
R	8.314	J mol^{-1} K^{-1}	–
$r^{(agg)}$	10^{-7}	m	[62]
$T^{amb}, T_a^{in}, T_{cool}^{in}, T_0$	298.15, 333.15, 333.15, 333.15, 298.15	K	–, [69]
u_a^{in}, u_c^{in}	1,2	m s^{-1}	[32]
W_{ff}, W_{fc}	$(2,3) \times 10^{-3}$	m	–
$\alpha_a^{ox}, \alpha_a^{rd}$	1,1	–	[31,56]
$\alpha_c^{ox}, \alpha_c^{rd}$	1.5, 1.5	–	[31]
$\beta^{(m)}$	0.7	–	[31]
$\varepsilon_{gdl}, \varepsilon_{cl}$	0.4, 0.4	–	[54]
θ	0	°	[54]
$k_{gdl}, k_{cl},$	$7{:}3 \times 10^{-13}, 7.3 \times 10^{-13}$	m^2	[54]
$\mu^{(1)}$	4.7×10^{-4}	kg m^{-1} s^{-1}	[54]
$\mu_{H_2}^{(g)}, \mu_{H_2O}^{(g)}, \mu_{N_2}^{(g)}, \mu_{O_2}^{(g)}$	$(0.841, 1.34, 1.663, 1.919) \times 10^{-5}$	kg m^{-1} s^{-1}	[67]
$\rho^{(C)}, \rho^{(1)}, \rho^{(m)}, \rho^{(Pt)}$	$(1.8, 0{:}983, 2, 21.45) \times 10^3$	kg m^{-3}	[54,62]
$\rho_{cl}, \rho_{gdl}, \rho_{bp}$	$(5.28, 0.5, 8, 02) \times 10^3$		[62,66]
$\sigma_{eff,cl}^{(s)}, \sigma_{eff,gdl}^{(s)}, \sigma_{eff,bp}^{(s)}$	$500, 500, 1.37 \times 10^6$	S m^{-1}	[54,66]
τ	6.25×10^{-2}	N m^{-1}	[31]
$\omega^{(Pt)}$	0.4	–	[31]
c_1, c_2	$-2.1794, 2.953 \times 10^{-2}$	–, K^{-1}	[43]
c_3, c_4	$-9.1837 \times 10^{-5}, 1.4454 \times 10^{-7}$	K^{-2}, K^{-3}	[43]
ℓ_1	-9×10^{-4}	V K^{-1}	[56]
$\mathcal{L}^{(p)}, \mathcal{L}^{(Pt)}$	$10^{-2}, 0.3 \times 10^{-3}$	kg m^{-2}	[54]
$\mathfrak{H}_a^{in}, \mathfrak{H}_c^{in}, \mathfrak{H}^{amb}$	100, 100, 50	%	[54] [32]
$\mathfrak{T}_0, \mathfrak{T}_1, \mathfrak{T}_2$	273.15, 353.15, 298.15	K	[56]

each case. The base–case parameters and its operating conditions are presented in Table 4.

4.1. Case (i): liquid-cooled stack

This part examines a PEFC stack with liquid coolant plates at the top and bottom of each cell (see Fig. 2a). Five different coolant flow rates, which correspond to Reynolds numbers ~ 10, 25, 50, 75 and 100, are simulated to study the impact of coolant flow rate on thermal management and stack performance. Generally, increasing the coolant flow rate increases the heat transfer rate, for which it is expected to be able to maintain the thermal envelope of the stack [38]. This is indeed the case, as can be seen from Fig. 3a; increasing coolant flow

rate enhances the stack performance. It is noted that at a cell voltage of 0.6 V, the current density almost doubles as the coolant flow rate increases from Re ~ 10 to 100. This improvement is insignificant when the coolant flow rate increases from Re 75 to 100, especially at lower current densities. A plausible explanation is the fact that the current density approaches a limiting value; that is an increase in heat removal rate does not give any improvement in stack performance. Furthermore, as expected, increasing the coolant flow rate improves the heat transfer rate as mirrored by reduction in the stack temperature; the maximum stack temperature decreases from 87 to 67 °C when the coolant flow rate increase from Re ~10 to 100; however, there is no significant difference (~1 °C) when the coolant flow rate increases from Re ~75 to
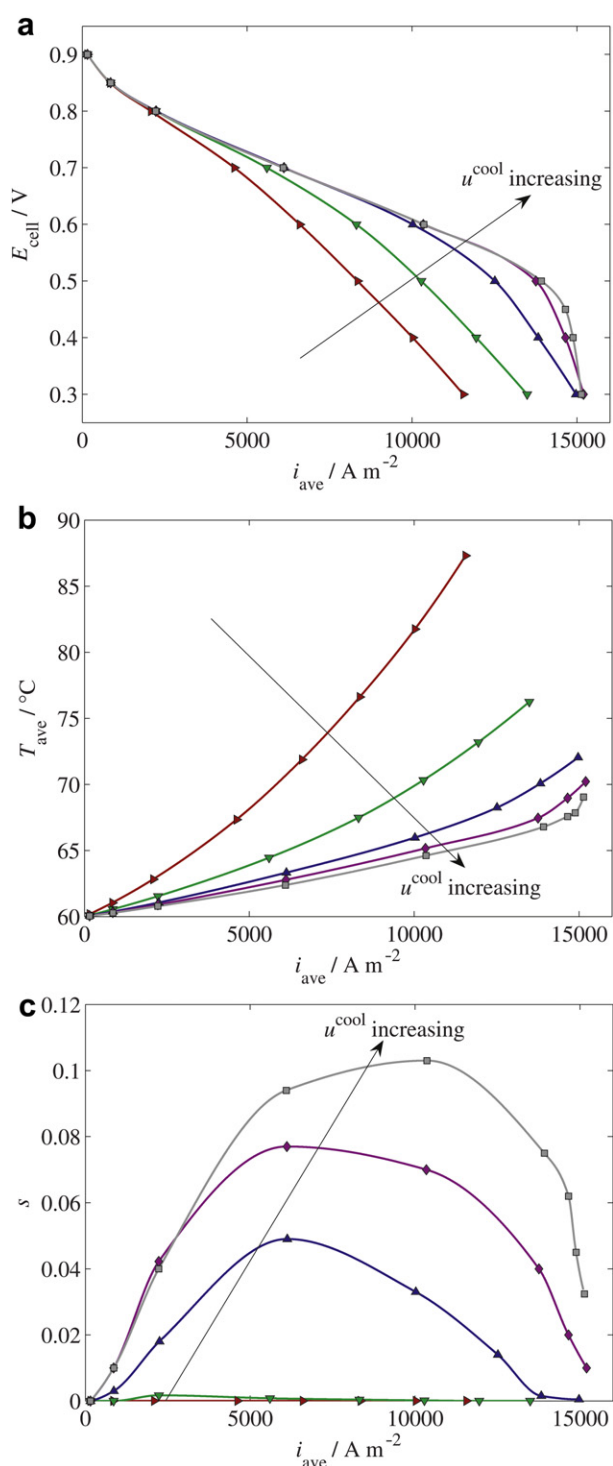
Fig. 3 — Comparison of a) polarization curve; b) average stack temperature; c) average liquid saturation at the cathode gas diffusion and catalyst layers for liquid coolant Re of 10 (▶), 25 (▼), 50 (▲), 75 (◆), and 100 (■).

100, as can be inferred from Fig. 3b. As thermal management is directly linked to water management, it is of interest to look at the membrane water content and liquid saturation. For the former, the membrane water content and protonic

conductivity at a coolant flow rate Re $\sim$ 10 is found to be half to that at Re $\sim$ 75 and 100. This indicates that at low coolant flow rates the membrane is drying up; whereas at high coolant flow rate the membrane remains sufficiently hydrated. Moreover, the difference of membrane water content between coolant flow rate with Re 75 and 100 is found to be only about 5% at cell voltage of 0.4 V; it is therefore of interest to look closer to the amount of liquid saturation at the gas diffusion and catalyst layer to determine an "ideal" coolant conditions to ensure membrane at right humidification level. Fig. 3c shows the computed average liquid saturation values at the cathode gas diffusion layer and catalyst layer. It is observed that the average liquid saturation for coolant at Re $\sim$ 100 yields the highest value among others (up to 10% at current density 10,000 A m^{-2}). This is due to the fact that higher coolant flow rate removes more heat from the stack which lower the stack temperature (see Fig. 3b); on the other hand, more water is being produced due to electrochemical reaction at the cathode side; if the water vapor partial pressure exceeds the saturation pressure, it causes more water vapor to condense. It is also noted that the liquid saturation decreases gradually when the current density is increased further: more heat and water are generated at higher current density; as heat removal rate is kept constant, it will reach a point where water vapor partial pressure is equal, and then lower than the water saturation pressure; thus, a lower condensation rate is obtained. There is thus scope for improving stack performance further by adjusting the coolant flow rate: too low a coolant flow rate causes membrane dry-up which deteriorates stack performance; conversely, too high a coolant flow rate can cause water vapor partial pressure exceeds the saturation pressure which lead to a condensation (or flooding) and lower stack performance. In addition, high flow rate causes high pressure drop and hence a high parasitic load (pumping power). Careful balance has to be taken by fine-tuning various operating parameters, e.g., coolant flow rate, operating voltage, and stack temperature to achieve high performance PEFC stack. In this particular case for example, a coolant flow rate of $\sim$75 with operating cell voltage of 0.6 V produces current density 10,000 A m^{-2} and average temperature increase of $\sim$5 °C which was found to be a near-to- or optimum operating condition.

4.2. Case (ii): air-cooled stack

Liquid water has been widely used as the coolant fluid due to its high thermal conductivity and heat capacity. However, it requires high pumping power to drive the flow as it has high viscosity and density. Moreover, if it is used as a coolant fluid for fuel cell stacks, it will require additional equipment such as coolant loop, heat exchanger, and pump to be included to the system which increase complexity, cost, size and weight. In some application, e.g., small automotive, these become a limiting factor which reduce the flexibility of fuel cell applications. Hence, to overcome these issues, air is considered as a coolant fluid to replace liquid water; coolant loop and heat exchanger is therefore not required in the system. In this study, the stack model used in case (i) is modified by replacing the coolant fluid into air, three different coolant flow rates corresponding to Re $\sim$ 100, 500, and 1000 are investigated.
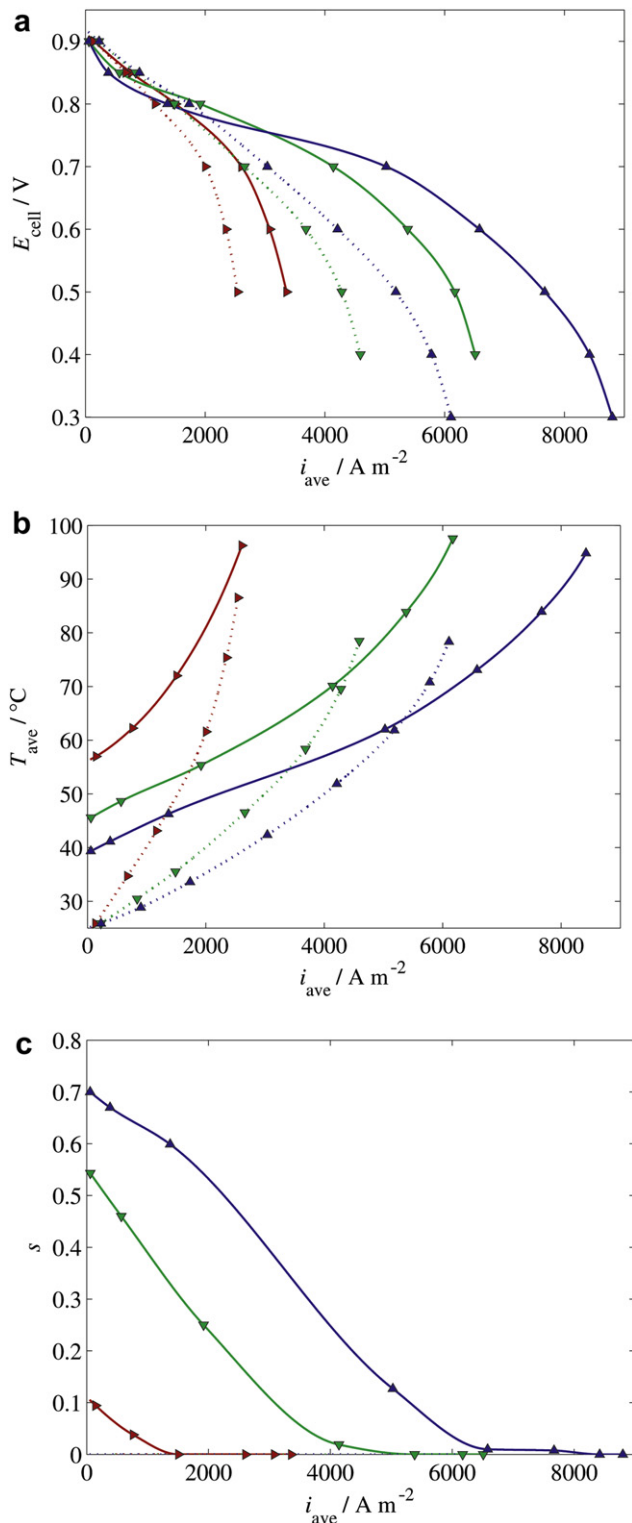
Fig. 4 − Comparison of a) polarization curve; b) average stack temperature; c) average liquid saturation at the cathode gas diffusion and catalyst layers for air coolant Re of 100 (▶), 500 (▽), and 1000 (▲) with inlet gas (fuel and oxidant) temperature at 60 C [−] and 25 C [⋯].
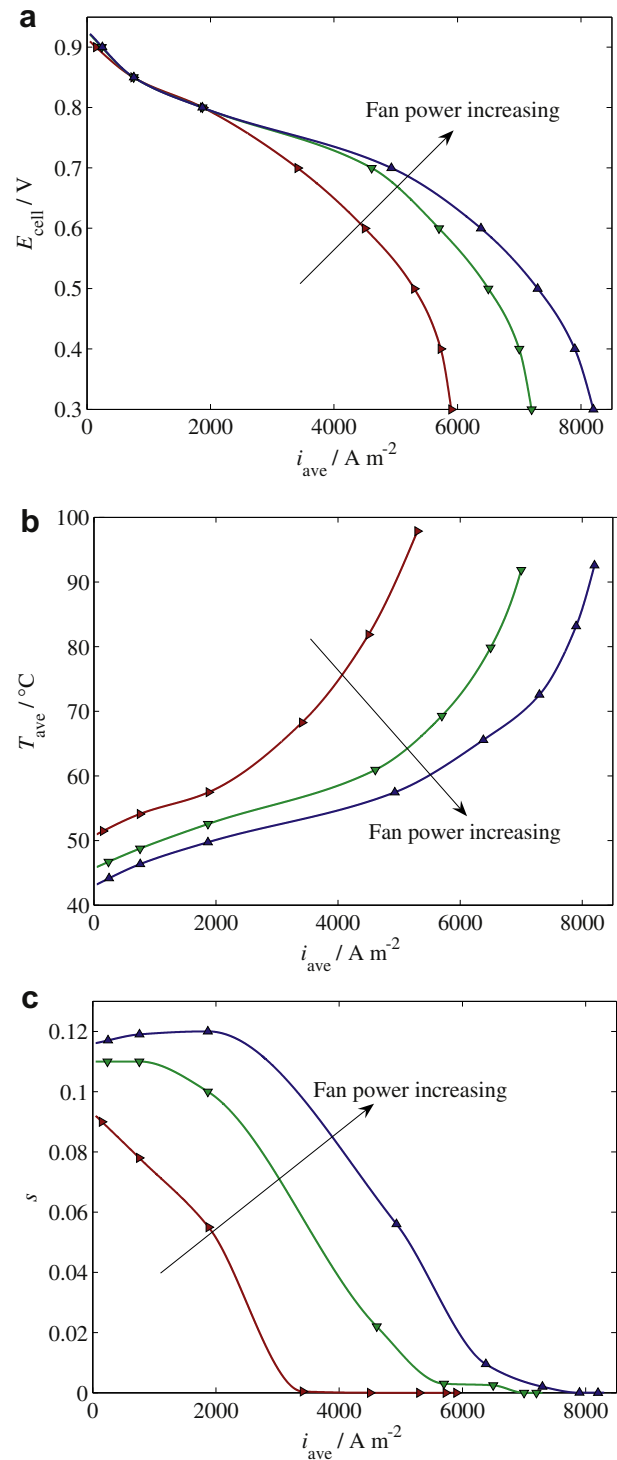
Fig. 5 − Comparison of a) polarization curve; b) average stack temperature; c) average liquid saturation at the cathode gas diffusion layer and catalyst layer for edge-cooling with fan power of 4.5 (▶), 19.5 (▽), and 30 W (▲).

Similar to liquid cooling, the results indicate that increasing air flow rate improves stack performance, as can be inferred from Fig. 4a. It is noted that the limiting current density improves up to two-fold by increasing the air flow rate ten-fold. This improvement is mainly caused by a lower stack

temperature (see Fig. 4b); the temperature falls to about 45 °C at a current density of 2200 A m^{-2} when the air flow rate increases by one order-of-magnitude. However, the stack performance at low current density (≤1800 A m^{-2}) is found to be lower at higher air coolant flow rate. At low current density, the amount of heat generation is less; whereas, at higher air coolant flow rate, more heat is being dissipated. Since the ambient air temperature is lower than the stack operating temperature, this brings the stack temperature down below its operating temperature (in this particular case is 60 °C). At very low current density (∼0 A m^{-2}), the higher the air flow rate results in lower stack temperature (see solid line in Fig. 4b) due to higher heat dissipation rate; however, this is not the case when the gas inlet temperature is equal to ambient temperature (see dotted line in Fig. 4b) as it has already reached isothermal condition. Furthermore, as fuel and oxidant at the inlet are pre-conditioned (fully humidified and heated at operating temperature), excessive cooling leads to increased condensation inside the stack, as can be seen in Fig. 4c. This condensation phenomena at lower current densities can be avoided by, for example, decreasing coolant flow rate, reducing anode and cathode inlet humidification, or lowering inlet gas (fuel and oxidant) temperature. The latter is shown in the dotted line in Fig. 4 for which the inlet gas temperature is assumed to be the same as ambient temperature. In contrast to the case with heated gas inlet condition, the polarization curve at both high and low current density have similar trend (Fig. 4a): the stack performance is higher at higher air coolant flow rate. We also note that at higher current density, the stack performance for heated gas inlet is higher up to around 30%. This is attributed to the higher stack operating temperature (Fig. 4b) which is beneficial for faster reaction kinetics. Conversely, at lower current density the performance of case with heated gas inlet is lower (∼ 20%) due to higher liquid saturation (Fig. 4c). Therefore, it can be deduced that unheated gas inlet is recommended for air-cooled stack operate at low current density, whereas heated gas inlet is preferred when stack operates at high current density. In addition, to maintain stack from overheating at higher current densities, one can increase the air flow rate or design a larger coolant channel to allow more air flow to remove heat [8,47]. An innovative design by utilizing heated air from coolant outlet to be used as oxidant has also been implemented [48].

4.3. Case (iii): edge-cooled stack

In a stack with specially designed coolant plates, the coolant is distributed over the entire active area through the channels; this allows for local heat removal which reduces the temperature gradient. However, this adds to the complexity of the design, contributes to higher initial cost due to channel machining, and higher operating costs due to high pumping power to drive the coolant flow in the small channels. Edge-cooling, where fins are attached to the stack surface to enhance heat transfer from the fuel cell to the ambient, has received attention as a promising strategy to overcome these issues [16]. Here, the stack model used in cases (i) and (ii) is extended to account for fins, ambient and fan (see Fig. 2b). All the geometries, operating conditions and physical parameters are similar, except that the separator plates are extended in the spanwise direction to form fins. Moreover, the fan is resolved as an interfacial condition with the polynomial expression for the static pressure increase over the fan as a function of the fan velocity. Three different fan power ratings from [49], namely, 4.5, 19.5 and 30 W, are simulated. The results indicate that increasing fan power rating−which implies to a higher air flow rate−gives rise to better stack performance and reduced average stack temperature, as can be seen in Fig. 5a and b, respectively. At low current density (≤2000 A m^{-2}), however, increasing fan power does not give rise to a discernable difference in stack performance, though the average stack temperature differ by about 8 °C. Now, looking to the average liquid water saturation inside the gas diffusion and catalyst layers (see Fig. 5c), the highest saturation (up to 12% higher) is found for the case with the highest fan power rating (30 W) at current density ≤ 2000 A m^{-2}. This value is much lower than that for the air-cooling case presented in Sub-section 4.2 for which the liquid saturation goes up to about 60%. It is noted that an elevated temperature at the middle of the stack prevents water vapor to condense; whereas for the air-cooling case, the uniform coolant flow through coolant plate causes excessive cooling which leads the water vapor to condense. This, therefore, becomes an advantage for edge-cooling when operated at low current densities; at high current densities, however, a significant temperature gradient can develop in the middle of the stack due to non-uniform cooling, which, in turn, deteriorates stack performance. To further improves stack thermal management from fins to

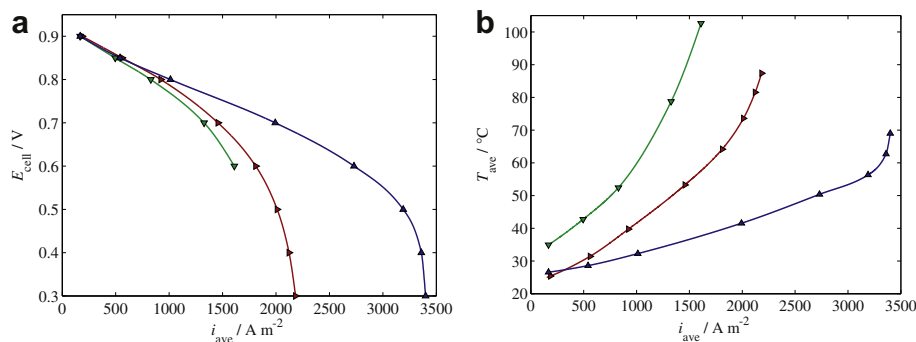Fig. 6 − Comparison of a) polarization curve; b) average stack temperature for single cell with natural convection (▶), stack with natural convection (▼), stack with forced air-convection (fan) cooling 4.5 W (▲).

ambient, one can design the fins made from highly conductive material, increase surface heat transfer (fins) area, adjust fan power rating and conduct fins geometrical optimization. This model can aid and help fuel cell engineer to determine the best design with regard to the stack performance, parasitic load, size and manufacturing cost.

4.4. Case (iv) and (v): open-cathode stacks

To reduce the complexity of the cooling system and inlet pre-conditioner (heater and humidifier), an open-cathode PEFC stack, in which the ambient air is directly used as both oxidant and coolant, is considered. The air flows can be provided by either forced (case iv) or natural convection (case v). For the case of a fuel cell single cell or stack operating at natural convection conditions, the removal rate is limited by the natural convection to and from the cell/stack. Generally, this only allows for the operation of small stacks of a few cells, depending on the stack size. In this study, an open-cathode PEFC stack comprising 12 cells is considered for both natural and forced convection powered by a 4.5 W fan from [49], as illustrated in Fig. 2c; moreover, the stack with natural convection (case v-a) is also compared with that of single cell (case v-b). The stack model is based on the closed manifold model, except that the cathode is now open to the ambient; whole cells in the stack are simulated without unit repetition assumption. The stack length and cathode channel height are assumed to be 5 cm and 3 mm which are typical geometries found in PEFC stack with open-cathode [19–21,50,51].

Earlier experimental studies [52] have shown that the performance of natural convection open-cathode stack is lower relative to that of forced convection. This is indeed the case, as can be seen in Fig. 6a, where stack with forced air-convection yields better performance, followed by natural convection single cell, and stack. The limiting current for forced convection cooling is seen to be twice that for natural convection stack performance. For a stack cooled by natural convection (case v-a), the polarization curve stops at current density ~1600 A m^{-2} at 0.6 V; whereas for case (v-b), the polarization can reach higher current density up to 2200 A m^{-2} at 0.3 V. This phenomena can be adequately explained by the fact that for the natural convection cooled stack (case v-a), stack temperature rises beyond its allowable operating value (>100 °C) at voltage lower than 0.6 V due to insufficient cooling (see Fig. 6b). The higher temperature inside each cell of the stack leads to a lower water content in the membranes and thus an increase in ohmic resistance, which in turn manifests itself in a lower performance. The temperature difference between natural convection single cell and the stack comprising of 12 cells is up to 40 °C in this particular case. From Fig. 7, one can see that the temperature distribution is similar to the thermal plume observed experimentally by [53]. Focusing on case v-b, and the immediate vicinity of the cell, as depicted in Fig. 7a, it is observed that the temperature rise in the fuel cell of up to ~20 °C at current density ~1600 A m^{-2} is close to the temperature observed experimentally for a single cell by Fabian et al. [53]. Moreover, a higher temperature of up to ~80 °C is observed for a stack cooled by natural convection, as portrayed in Fig. 7b whereas the lowest temperature is obtained in a stack cooled by forced convection (see Fig. 7c). As
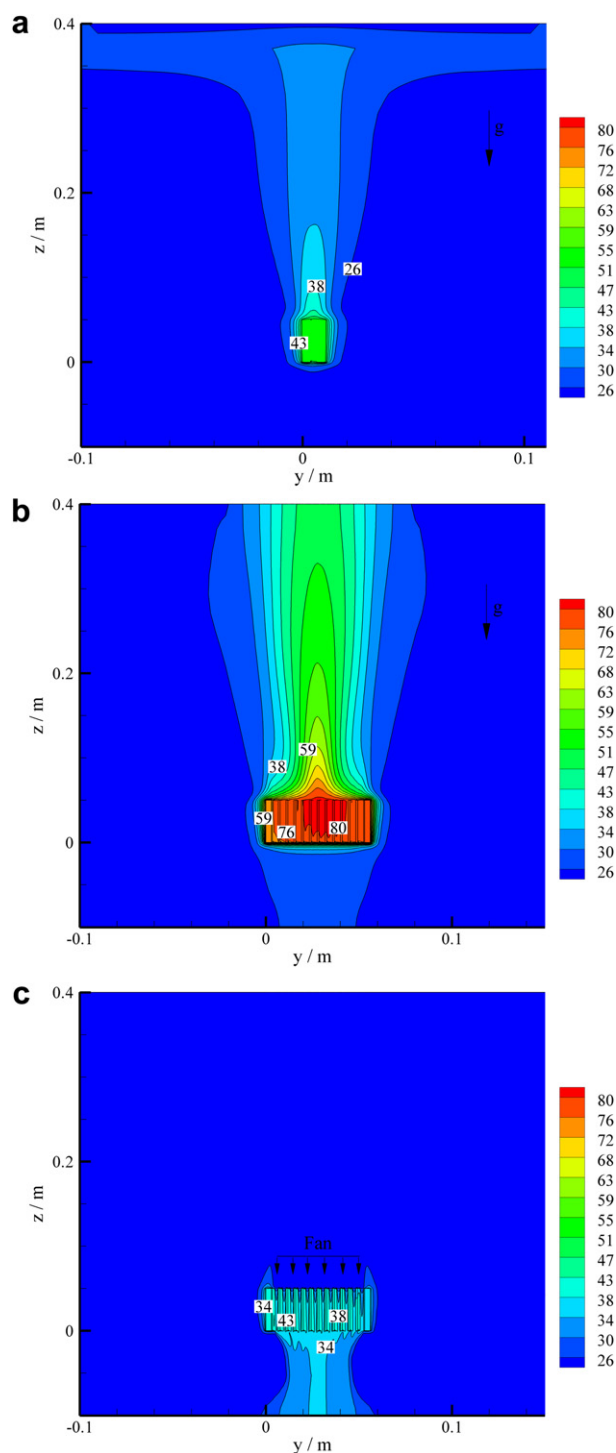
Fig. 7 – Thermal plume for a) single cell with natural convection; b) stack with natural convection; c) stack with forced air-convection (fan) cooling.

temperature is one of the driving forces for the density variations and buoyant flow in natural convection case, it is therefore of interest to evaluate the velocities at the cathode channels. It is observed that for single cell natural convection, the average air velocities at the cathode is slightly lower
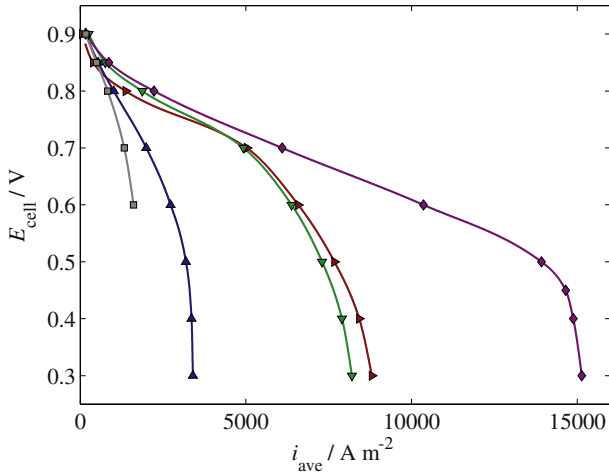
Fig. 8 — Polarization curves for PEFC stack with liquid cooling (♦); edge-cooling (▶); air cooling (▼); open-cathode with forced (▲) and natural-air-convection (■).

$(2 \times 10^{-2}$ m s$^{-1})$ as compared to that of stack $(3.5 \times 10^{-2}$ m s$^{-1})$. Whence higher velocity is beneficial to provide higher oxidant stoichiometry and heat removal rate, the velocity arise due to natural convection is still too low to provide sufficient cooling for stack as it is two-order magnitude lower than that of typical forced convection cooling [32]. Clearly, when designing an open-cathode stack cooled by natural convection, the number of cells in the stack should be considered carefully as overheating may arise due to insufficient heat removal. Thus, for open-cathode stack with a large number of cells, it is recommended to add fan(s) to avoid stack overheating.

4.5. Comparison of various cooling strategies

Thus far, we have examined five type of thermal management strategies with respect to the cooling condition aspect individually. Now, let us have a look at Fig. 8 which displays and compares the predicted stack performance for different thermal management strategies. Here, several features are apparent; foremost is that stack performance is greatly affected by the cooling strategy chosen. It is seen that liquid cooling yields the best results among various alternatives. The natural convection open-cathode stack gives the lowest performance. The computed limiting current density for each case is found to be similar to that found in published experimental investigation: liquid cooling up to 15,000 A m^{-2} [54], air-cooling up to 8000 A m^{-2} [29], edge-cooling up to 8500 A m^{-2} [16], and forced and natural convection with open-cathode up to 3500 A m^{-2} [19] and 1500 A m^{-2} (52), respectively. Conversely, when the complexity, cost, size, weight, and parasitic load are of interest, the order is reversed; for example, stack with liquid cooling requires a coolant loop, a radiator, a pump, more space and weight as well as additional costs to build the supporting equipment. Natural convection cooling, on the other hand, does not require any additional auxiliary equipment and hence is the least expensive. In practical applications, the fuel cell stack is typically operated at 0.6—0.7 V. It is therefore of interest to look closer to the performance in the operating voltage. Table 5 shows the predicted stack performance in terms of power per unit active area, power per unit stack volume and power per unit stack weight, at normalized cell voltage of 0.6 V. It is seen that increasing the coolant flow rate can improve the stack power and reduce the stack average temperature; however, this is not always the case for the net power, defined as stack power minus pumping power, as increasing coolant flow rate required higher pumping power which becomes a parasitic load to the stack itself. In this particular case for liquid-cooled stack, increasing coolant flow rate from Re ∼75 to 100 reduces the net power up to around 10%. In terms of power per unit catalyst active area and power per unit volume, liquid-cooled stack yields the best performance among others, followed by air-cooled, edge-cooled, open-cathode with forced convection and natural-convection. We note that edge-cooled stack requires larger total volume compared to liquid- and air-cooled stack as the bipolar plate is extended to form fins. Now looking

Table 5 — Summary of stack performance with various thermal management strategies at normalized cell voltage of 0.6 V.					
	P_{stack} (W m^{-2})	P_{cool} (W m^{-2})	P_{net} (W m^{-2})	P_{net} (W m^{-3})	P_{net} (W kg^{-1})
Liquid-cooled					
$Re_{cool} = 10$	3950	8	3942	6.95×10^5	138
$Re_{cool} = 25$	5000	50	4950	8.73×10^5	173
$Re_{cool} = 50$	6000	203	5797	1.02×10^6	203
$Re_{cool} = 75$	6205	305	5900	1.04×10^6	206
$Re_{cool} = 100$	6216	824	5392	9.51×10^5	189
Air-cooled					
$Re_{cool} = 100$	1850	1.5	1848.5	3.26×10^5	66
$Re_{cool} = 500$	3230	42	3188	5.62×10^5	114
$Re_{cool} = 1000$	3950	190	3760	6.63×10^5	134
Edge-cooled					
$P_{fan} = 4.5$ W	2640	22	2618	3.57×10^5	98
$P_{fan} = 19.5$ W	3360	96	3264	4.45×10^5	122
$P_{fan} = 30$ W	3830	148	3682	5.01×10^5	138
Open-cathode					
Forced convection	1640	35	1605	2.83×10^5	82
Natural convection	970	0	970	1.70×10^5	50

at the stack weight as it is one of the major constraint in automotive or mobile application, it is observed that the liquid-cooled stack is the heaviest ($\rho_{stack} \sim 5050$ kg m^{-3}) among others, followed by air-cooled ($\rho_{stack} \sim 4950$ kg m^{-3}), edge-cooled ($\rho_{stack} \sim 3650$ kg m^{-3}) and open-cathode stack ($\rho_{stack} \sim 3400$ kg m^{-3}). Interestingly, edge-cooled stack is lighter than air-cooled although it has larger total volume; this is attributed to the fact that the volume in between fins is an empty space for air to flow which does not add weight to the stack. Proceeding to the power per unit stack weight, it is noted that the performance of edge-cooled stack is somewhat higher ($\sim 10\%$) as compared to air-cooled stack. This indicates that edge-cooled has potential advantages, i.e., lighter and higher performance, for thermal management in application where weight is the main constraint, e.g. automotive or mobile applications. Of course, further optimization may be needed for specific application. The manufacturing cost, performance, and durability would decide the selection between these strategies. In addition, combination of several alternatives, e.g. forced- or natural-convection open-cathode with fins or combination of air-cooled and edge-cooled, can also be considered to improve the stack performance further.

5. Conclusions

A computational study of PEFC stacks with various cooling strategies, namely, liquid cooling, air cooling, edge-cooling, forced and natural convection in open-cathode has been developed and carried out, where the comprehensive mechanistic model comprised of PEFC stack, coolant plates, ambient, fan and fins are resolved in details. It is shown that liquid cooling yields best performance among the alternative designs examined. This is due to its ability to maintain a better stack thermal envelope as compared to edge-cooling, air-cooling and natural convection cooling. Natural convection air cooling is only marginally able to maintain the temperature for stacks with a large number of cells.

It has been shown that coolant flow rate significantly affect the net power generated; one needs to balance between heat dissipation rate, stack performance and parasitic load. For liquid-cooled stack, coolant flow rate at Re ~ 75 is found to be close-to-optimum value in this particular case. For air-cooled stack, heated and humidified gas (fuel and oxidant) inlet is recommended at high current density operation; whereas unheated inlet gas with low humidification is suggested at low current density operation to avoid condensation. Edge-cooled stack is found to have potential for automotive/mobile application due to its relatively high performance, simplicity of the design and lighter as compared to air-cooled stack – of course, further optimization may be needed for specific applications. Natural convection cooling is only able to maintain thermal envelop for single cell or stack within few cells; if more cells, e.g., 12 cells, are placed inside the stack, it is suggested to add fan to assist in removing heat and supplying oxidant.

Clearly, several considerations have to be taken into account when selecting thermal management strategies for fuel cell stacks as one may add complexity, parasitic load, size, weight, and cost which can be impractical in real application. The mathematical model derived here and subsequent numerical implementation allow for wide-ranging parameters and optimization studies such as stack design (flow channel and manifold design, geometrical parameters including size and weight of the stack, number of cells in stack, etc.), parasitic loads (fan/blower/compressor selection), and operating parameters (temperature, humidity, flow rate, stoichiometry, etc.), that can aid in the selection of the thermal management system for a specific application.

Acknowledgments

Nomenclature

a	water activity
$a^{(l)}$	surface area of the agglomerates including water per unit volume, m^{-1}
$a^{(p)}$	surface area of the agglomerates per unit volume of catalyst layer, m^{-1}
A_{cl}	catalyst area, m^2
A_{fan}	total area of the fan, m^2
$c_i^{(g)}$	molar concentration of species i, mol m^{-3}
$c_{i,ref}^{(g)}$	reference molar concentration of species i, mol m^{-3}
$c_p^{(g)}$	specific heat capacity of gas mixture, J kg^{-1} K^{-1}
$c_{p_i}^{(g)}$	specific heat capacity of species i, J kg^{-1} K^{-1}
c_r	condensation/evaporation rate constant, s^{-1}
$\mathfrak{C}_1, \mathfrak{C}_2, \mathfrak{C}_3, \mathfrak{C}_4, \mathfrak{C}_5, \mathfrak{C}_6, \mathfrak{C}_7, \mathfrak{C}_8$ constants for the fan characteristic curve; Pa s^7 m^{-7}, Pa s^6 m^{-6}, Pa s^5 m^{-5}, Pa s^4 m^{-4}, Pa s^3 m^{-3}, Pa s^2 m^{-2}, Pa s m^{-1}, Pa	
c_1, c_2, c_3, c_4 constants for the saturation pressure of water; -, K^{-1}, K^{-2}, K^{-3}	
$D_i^{(g)}$	diffusivity of species i, m^2 s^{-1}
$D_{H_2O}^{(m)}$	diffusivity of water in the membrane, m^2 s^{-1}
$D_{O_2,eff}^{(agg)}$	effective diffusion coefficient of oxygen in the ionomer inside the agglomerate, m^2 s^{-1}
$D_{O_2}^{(l)}, D_{O_2}^{(p)}$	diffusion coefficient of oxygen in liquid water and in polymer film, m^2 s^{-1}
E_a	activation energy, J mol^{-1}
E_{cell}	cell voltage, V
E_{rev}	reversible cell potential, V
E_{stack}	stack voltage, V
$\mathbf{e}_x, \mathbf{e}_y, \mathbf{e}_z$	coordinate vectors
F	Faraday's constant, A s mol^{-1}
h	height, m
$H_{O_2}^{(l)}, H_{O_2}^{(p)}$	Henry's constant for air–water and air–polymer interfaces, Pa m^3 mol^{-1}
H_{vap}	heat of vaporization, J kg^{-1}
$\mathfrak{H}$	relative humidity, %
$i, \mathbf{i}$	current density, A m^{-2}
$j_{a,c}^{ref}$	anode and cathode volumetric reference exchange current density, A m^{-3}
J	volumetric current density, A m^{-3}
$\mathscr{J}$	Leverett function

k	thermal conductivity, W m^{-1} K^{-1}
k_c	reaction rate constant, s^{-1}
L	length, m
t_1	constant, V K^{-1}
$\mathfrak{L}^{(C)}, \mathfrak{L}^{(p)}, \mathfrak{L}^{(Pt)}, \mathfrak{L}^{(p)}$	carbon, polymer, and platinum loading, kg m^{-2}
$\dot{m}_{H_2O}$	interphase mass transfer due to condensation or evaporation of water, kg m^{-3} s^{-1}
$M^{(g)}$	mean molecular mass of the gas phase, kg mol^{-1}
M_i	molecular mass of species i, kg mol^{-1}
$M^{(m)}$	equivalent weight of the dry membrane, kg mol^{-1}
$n^{(agg)}$	number of agglomerates per unit volume, m^{-3}
n_{cell}	number of cells in the stack
n_d	electroosmotic drag coefficient
$\mathbf{n}_i^{(g)}$	mass flux of species i, kg m^{-2} s^{-1}
$p^{(c)}, p^{(g)}$	capillary and gas pressure, Pa
$p_{H_2O}^{sat}$	saturation pressure of water, Pa
R	gas constant, J mol^{-1} K^{-1}
$r^{(agg)}$	radius of agglomerate, m
s	liquid saturation
S	source term
$\mathfrak{T}_0, \mathfrak{T}_1, \mathfrak{T}_2$	constants, K
T	temperature, K
$\mathbf{u}, u, v, w, U$	velocities, m s^{-1}
V	volume, m^3
W	width, m
$x_i^{(g)}$	molar fraction of species i
x, y, z	coordinates, m
$\omega_i^{(g)}$	mass fraction of species i
$\omega^{(p)}$	mass fraction of polymer loading
$\omega^{(Pt)}$	mass fraction of platinum loading on carbon

Greek

α	transfer coefficient
$\beta^{(m)}$	modification factor
γ	volume fraction
δ	thickness of the film, m
$\mathbf{\Delta}$	difference
ε	porosity
η	overpotential, V
θ	wetting angle
κ	permeability, m^2
λ	water content
μ	dynamic viscosity, kg m^{-1} s^{-1}
ξ	stoichiometry
ξ_1, ξ_2, ξ_3	correction factors for the agglomerate model
ρ	density, kg m^{-3}
τ	surface tension, N m^{-2}
$\boldsymbol{\sigma}$	total stress tensor, N m^{-2}
$\sigma^{(m)}$	protonic conductivity, S m^{-1}
$\sigma^{(s)}$	electric conductivity, S m^{-1}
$\phi^{(m)}$	ionic phase potential, V
$\phi^{(s)}$	solid phase potential, V
$\Phi_{\alpha\beta}$	dimensionless quantities
Φ	Thiele modulus

Superscripts

(agg)	agglomerate
(c)	capillary
(cool)	coolant
(C)	carbon
(g)	gas phase
in	inlet
(l)	liquid phase
(m)	membrane
ox	oxidation
(p)	polymer phase
(Pt)	platinum
(PtC)	platinum and carbon
rd	reduction
ref	reference
(s)	solid
sat	saturation

Subscripts

α, β	index for species
a	anode
amb	ambient
ave	average
bp	bipolar plate
c	cathode
cc	current collector
cell	cell
cl	catalyst layer
cp	coolant plate
eff	effective
fan	fan
fin	fin
fc	fuel cell
ff	flow channel
gdl	gas diffusion layer
H_2	hydrogen
H_2O	water
i	species i
j	functional layer j
m	membrane
mass	mass
net	net
N_2	nitrogen
O_2	oxygen
pot	potential
ref	reference
stack	stack
std	standard deviation
temp	temperature
tot	total
void	void
0	standard conditions

REFERENCES

[1] Chang PAC, Pierre JS, Strumper J, Wetton B. Flow distribution in proton exchange membrane fuel cell. J Power Sources 2006;162:340–55.

[2] Dhathathreyan KS, Rajalakshmi N. In: Basu S, editor. Polymer electrolyte membrane fuel cell, book chapter in: recent trends in fuel cell science and technology. Anamaya Publisher; 2007.

[3] Larminie J, Dicks A. Fuel cell systems explained. 2nd ed. Wiley; 2003.

[4] Faghri A, Guo Z. Challenges and opportunities of thermal management issues related to fuel cell technology and modeling. Int J Heat Mass Transfer 2005;48:3891—920.

[5] Kandlikar SG, Lu Z. Thermal management issues in a PEMFC stack - a brief review of current status. Appl Therm Eng 2009; 29:1276—80.

[6] Faghri A. Unresolved issues in fuel cell modeling. Heat Transfer Eng 2006;27:1—3.

[7] Kandlikar SG, Lu Z. Fundamental research needs in combined water and thermal management within a proton exchange membrane fuel cell stack under normal and cold-start conditions. J Fuel Cell Sci Technol 2009;6: 044001—13.

[8] Von Helmot R, Lehnert W. Air-cooled PEM fuel cells. In: Vielstich W, Gasteiger H, Lamm A, editors. Handbook of fuel cells - fundamentals, technology and applications. Wiley; 2003.

[9] Chen CY, Lai WH, Weng BJ, Chuang HJ, Hsieh CY, Kung CC. Planar array stack design aided by rapid prototyping in development of air-breathing PEMFC. J Power Sources 2008; 179:147—54.

[10] Eckl R, Zehtner W, Liu C, Wagner U. Experimental analysis of water management in a self humidifying polymer electrolyte fuel cell stack. J Power Sources 2004;138:137—44.

[11] Rodatz P, Buchi F, Onder C, Guzzela L. Operational aspects of a large PEFC stack under practical condition. J Power Sources 2004;128:208—17.

[12] Laurencelle F, Chahire R, Hamelin J, Agbossou K, Bose TK, Laperriere A. Characterization of a Ballard MK5-E proton exchange membrane fuel cell stack. Fuel Cells 2001;1:66—71.

[13] Cheong S, Kim T, Kim D, Lee J, Hwang Y. Analysis of water and thermal management with coolant operating conditions for a proton exchange membrane fuel cell. Curr Appl Phys 2010;10:S22—s25.

[14] Yim SD, Sohn YJ, Yoon YG, Um S, Kim CS, Lee WY. Operating characteristic of 40W class PEMFC stack using reformated gas under low humidifying conditions. J Power Sources 2008; 178:711—5.

[15] Sohn YJ, Park GG, Yang TH, Yoon YG, Lee WY, Yim SD, et al. Operating characteristic of an air cooling PEMFC for portable applications. J Power Sources 2005;145:604—9.

[16] Fluckiger R, Tiefenauer A, Ruge M, Aebi C, Wokaun A, Buchi FN. Thermal analysis and optimization of a portable edge-air-cooled PEFC stack. J Power Sources 2007;172:324—33.

[17] Garrity P, Klausner J, Mei R. Flow boiling microchannel evaporator plate for fuel cell thermal management. Heat Transfer Eng 2007;28:877—84.

[18] Goebel SG. Evaporative cooled fuel cell; 2004. United States Patent No. US2004/0170878A1.

[19] Wu J, Galli S, Lagana I, Pozio A, Monetelone G, Yuan XZ. An air-cooled proton exchange membrane fuel cell with combined oxidant and coolant flow. J Power Sources 2009; 188:199—204.

[20] Jung GB, Lo KF, Su A, Weng FB, Tu CH, Yang TF, et al. Experimental evaluation of an ambient forced-feed air-supply PEM fuel cell. Int J Hydrogen Energy 2008;33:2980—5.

[21] Rosa DTS, Pinto DG, Silva VS, Silva RA, Rangel CM. High performance stack with open-cathode at ambient pressure and temperature conditions. Int J Hydrogen Energy 2007;32: 4350—7.

[22] Zang X, Wang T, Zhen D, Zhang J, Zhang Y, Zhu L, et al. Design, fabrication and performance characterizations of a miniature PEMFC stack based on MEMS technology. Int J Electrochem Sci 2007;2:618—26.

[23] Chu D, Jiang R. Performance of polymer electrolyte membrane fuel cell PEMFC stacks part 1. evaluation and simulation of an air-breathing PEMFC stack. J Power Sources 1999;83:128—33.

[24] Hottinen T, Himanen O, Lund P. Effect of cathode structure on planar free-breathing PEMFC. J Power Sources 2004;138: 205—10.

[25] Liu Z, Mao Z, Wang Z, Zhuge W, Zhang Y. Numerical simulation of a mini PEMFC stack. J Power Sources 2006;160: 1111—21.

[26] Shan Y, Choe SY. Modeling and simulation of a PEM fuel cell stack considering temperature effects. J Power Sources 2006; 158:274—86.

[27] Shan Y, Choe SY, Choi SH. Unsteady 2d PEM fuel cell modeling for a stack emphasizing thermal effects. J Power Sources 2007;165:196—209.

[28] Adzakpa KP, Ramousse J, Dube Y, Akremi H, Agbossou K, Dostie M, et al. Transient air cooling thermal modeling of a PEM fuel cell. J Power Sources 2008;179:164—76.

[29] Shimpalee S, Ohashi M, Zee JWV, Ziegler C, Stoeckmann C, Sadeler C, et al. Experimental and numerical studies of portable PEMFC stack. Electrochim Acta 2009;54:2899—911.

[30] Philipps SP, Ziegler C. Computationally efficient modeling of the dynamic behaviour of a portable PEM fuel cell stack. J Power Sources 2008;180:309—21.

[31] Sasmito AP, Birgersson E, Mujumdar AS. Numerical investigation of liquid water cooling for a proton exchange membrane fuel cell stack. Heat Transfer Eng 2011;32:151—67.

[32] Sasmito AP, Lum KW, Birgersson E, Mujumdar AS. Computational study of forced air-convection in open-cathode polymer electrolyte fuel cell stacks. J Power Sources 2010;195:5550—63.

[33] Matian M, Marquis A, Brandon NP. An experimentally validated heat transfer model for thermal management design in polymer electrolyte membrane fuel cells. J Power Energ 2010;224:1069—81.

[34] Matian M, Marquis A, Brett D, Brandon NP. Application of thermal imaging to validate a heat transfer model for polymer electrolyte fuel cells. Int J Hydrogen Energy 2010;35: 12308—16.

[35] Chen FC, Gao Z, Loufty RO, Hect M. Analysis of optimal heat transfer in a PEM fuel cell cooling plate. Fuel Cells 2003;3: 181—8.

[36] Real AJD, Arce A, Bordons C. Development and validation of a PEM fuel cell dynamic model. J Power Sources 2007;172: 310—24.

[37] Yu SH, Sohn S, Nam JH, Kim CJ. Numerical study to examine the performance of multi-pass serpentine flow-fields for cooling plates in polymer electrolyte membrane fuel cells. J Power Sources 2009;194:697—703.

[38] Kurnia JC, Sasmito AP, Mujumdar AS. Numerical investigation of laminar heat transfer performance of various cooling channel designs. Appl Therm Eng 2011;31: 1293—304.

[39] Li S, Becker U. A three dimensional CFD model for PEMFC. In: ASME Fuel Cell Science, editor. Proceeding of the second engineering and technology conference, vol. 2; 2004. p. 157—64. Rochester, NY.

[40] Schwarz DH, Djilali N. 3D modeling of catalyst layers in PEM fuel cells. J Electrochem Soc 2007;154:B1167—78.

[41] Sasmito AP, Mujumdar AS. Transport phenomena models for polymer electrolyte fuel cell stacks: thermal, water and gas management - from fundamentals to applications. Germany: Lambert Academic Publishing, ISBN 978-3-8443-9063-6; 2011.

[42] Bird RB, Stewart WE, Lightfoot EN. Transport phenomena. 2nd ed. Wiley; 2002.

[43] Springer T, Zawodzinski TA, Gottesfeld S. Polymer electrolyte fuel cell model. J Electrochem Soc 1991;138: 2334—42.

[44] Ju H, Meng H, Wang CYA. single-phase, non-isothermal model for PEM fuel cells. Int J Heat Mass Transfer 2005;48: 1303—15.

[45] Sasmito AP, Birgersson E, Lum KW, Mujumdar AS. Fan selection and stack design for open-cathode polymer electrolyte fuel cell stacks. Renewable Energy in press, DOI: 10.1016/j.renene.2011.06.037.

[46] Fluent 6.3.26, http://www.fluent.com; 2008. cited.

[47] Matian M, Marquis A, Brandon NP. Model based design and test of cooling plates for an air-cooled polymer electrolyte fuel cell stack. Int J Hydrogen Energy 2011;36:6051—66.

[48] Yang Y, Kao PM, Hsiao FH. Cooling of air-cooled fuel cell system, http://www.ebmpapst.us; April 2009. United States Patent No. US2005/0008912A1 2005. ebmpapst fan.

[49] Wang Y, Ouyang M. Three-dimensional heat and mass transfer analysis in an air-breathing proton exchange membrane fuel cell. J Power Sources 2007;164:721—9.

[50] Zhang Y, Mawardi A, Pitchumani R. Numerical studies on an air-breathing proton exchange membrane PEM fuel cell stack. J Power Sources 2007;173:264—76.

[51] Urbani F, Squadrito G, Barbera O, Giacoppo G, Passalacqua E, Zerbinati O. Polymer electrolyte fuel cell mini power unit for portable application. J Power Sources 2007;169:334—7.

[52] Fabian T, Posner JD, O'Hayre R, Cha SW, Eaton JK, Prinz FB, Santiago JG. The role of ambient conditions on the performance of a planar, air-breathing hydrogen PEM fuel cell. J Power Sources 2006;161:168—82.

[53] Noponen N, Birgersson E, Ihonen J, Vynnycky M, Lundblad A, Lindbergh G. A two-phase non-isothermal PEFC model: theory and validation. Fuel Cells 2004;4:365—77.

[54] Natarajan D, Nguyen TV. A two-dimensional, two-phase, multicomponent, transient model for the cathode of a proton exchange membrane fuel cell using conventional gas distributors. J Electrochem Soc 2001;148:A1324—35.

[55] Ju H, Wang CY, Cleghorn S, Beuscher U. Non-isothermal modelling of polymer electrolyte fuel cells. I. Experimental validation. J Electrochem Soc 2005;152:A1645—53.

[56] Song D, Wang Q, Liu ZS, Navessin T, Eikerling M, Holdcroft S. Numerical optimization study of the catalyst layer of PEM fuel cell cathode. J Power Sources 2004;126:104—11.

[57] Yang WW, Zhao TS. A two-dimensional, two-phase mass transport model for liquid-feed DMFCs. Electrochim Acta 2007;52:6125—40.

[58] Parthasarathy A, Srinivasan S, Appleby J, Martin CRG. Temperature dependence of the electrode kinetics of oxygen reduction reaction at the platinum/Nafion interface: a microelectrode investigation. J Electrochem Soc 1992;139: 2334—42.

[59] Harvey D, Pharoah JG, Karan K. A comparison of different approaches to modelling the PEMFC catalyst layer. J Power Sources 2008;179:209—19.

[60] Mann RF, Amphlettand JC, Peppley BA, Thurgood CP. Henry's law and the solubilities of reactant gases in the modelling of PEM fuel cells. J Power Sources 2006;161:768—74.

[61] Rao RM, Bhattacharya D, Rengaswamy R, Choudhury SR. A two-dimensional steady state model including the effect of liquid water for a PEM fuel cell cathode. J Power Sources 2007; 173:375—93.

[62] Wang Y, Wang CY. A non-isothermal, two-phase model for polymer electrolyte fuel cells. J Electrochem Soc 2006;153: A1193—200.

[63] Karawacki E, Suleiman BM. Dynamic plane source technique for simultaneous determination of specific-heat, thermal-conductivity and thermal-diffusivity of metallic samples. Meas Sci Technol 1991;2:744—50.

[64] Vie PJS, Kjelstrup S. Thermal conductivities from temperature profiles in the polymer electrolyte fuel cell. Electrochim Acta 2004;49:1069—77.

[65] Padhy BR, Reddy RG. Performance of DMFC with SS 316 bipolar/end plates. J Power Sources 2006;153:125—9.

[66] Lide DR. CRC handbook of chemistry and physics. 89th ed. Boca Raton, FL.: CRC Press/Taylor and Francis; 2009.

[67] Himanen O, Hottinen T, Tuurala S. Operation of a planar free-breathing PEMFC in a dead-end mode. Electrochem Commun 2007;9:891—4.

[68] Birgersson E, Noponen M, Vynnycky M. Analysis of a two-phase non-isothermal model for a PEFC. J Electrochem Soc 2005;152:A1021—34.

[69] Han M, Xu JH, Chan SH, Jiang SP. Characterization of gas diffusion layers for PEMFC. Electrochim Acta 2008;53:5361—7.